

**Research Aircraft Observations of the
Mesoscale and Microscale Structure of a
Cold Front Over the Eastern Pacific Ocean**

Nicholas A. Bond

Joint Institute for the Study of the Atmosphere and Ocean
University of Washington
Seattle, Washington 98195

M. A. Shapiro

National Oceanic and Atmospheric Administration
Wave Propagation Laboratory
Boulder, Colorado 80303

December 1990



QC
880.4
1f7
B71
1990

ABSTRACT

This study describes the structure of an oceanic cold front from research aircraft observations taken during the OCEAN STORMS field experiment. Synoptic and mesoscale analyses compare the structure of the upper-level jet-front system slightly downstream from the wind speed maximum (exit region) to its structure in the upstream entrance region. Stratospheric potential vorticity and ozone was found within the frontal zone down to ~800 mb. Microscale analyses of the front near the sea surface were carried out for a portion of the front having the signature of a "rope" cloud (shallow cumulus line) in satellite imagery. A narrow (<1 km) zone of upward motion ($\sim 4 \text{ m s}^{-1}$) and of horizontal shear ($\sim 10^{-2} \text{ s}^{-1}$) characterized the front near the surface. Significant along-front variability was found, including lateral displacements in the frontal zone where there were weaker updrafts; similar structures have been previously observed along precipitating fronts using Doppler radar. Pressure perturbations measured directly by the aircraft resemble pressure perturbations for a deeper, precipitating front that were derived indirectly from Doppler radar data. Results show that the frontal zone was well-defined through the depth of the troposphere, tapering from a width of ~100 km in the upper troposphere to ~1 km at the surface. The collapse of the front to such a narrow scale within the boundary layer occurred in the absence of precipitation, and obviously, in the absence of topographical influences.

LIBRARY
JAN 25 2006
National Oceanic &
Atmospheric Administration
U.S. Dept. of Commerce

1. Introduction

During the past two decades, the detailed structure of fronts has been studied using observing systems with high spatial and temporal resolution. It is a challenge to relate these past measurements to the evolving dynamical treatments of fronts. We first review some observational and theoretical studies of the fine-scale structure of fronts, and indicate how the present case study fits into the mosaic.

Doppler radar studies (e.g., Browning and Harrold 1970) have shown that a narrow line of forced moist convection often occurs at the leading edge of strong surface cold fronts. Fast-response instruments on meteorological towers have documented surface fronts with windshifts and temperature changes over horizontal scales as small as a few hundred meters (Shapiro 1984). Wind profiler measurements have provided the opportunity to study the details of kinematic fields associated with upper-tropospheric fronts (Larsen and Röttger 1982; Shapiro et al. 1984) and recently, with surface fronts (Neiman et al. 1990). Finally, research aircraft have probed both upper-tropospheric fronts (e.g., Shapiro 1974) and low-level cold fronts (e.g., Bond and Fleagle 1985).

Theoretical studies have addressed issues related to the dynamics and fine-scale structure of fronts. The semigeostrophic theory outlined by Sawyer (1956) and Eliassen (1959, 1962) provided a framework for diagnosing the ageostrophic circulations associated with frontogenesis. The analytical model of Hoskins and Bretherton (1972) showed that the semigeostrophic framework could account for the collapse of a baroclinic zone into a front of infinitesimal width in a finite time. This scale contraction was also modeled by the primitive-equation numerical simulations of Williams (1974) and Williams et al. (1981), among others. The mesoscale numerical simulations by Keyser and Anthes (1982) and Hsie et al. (1984) showed the importance of boundary layer processes and latent heating, respectively, on the evolution of lower tropospheric fronts. Gall et al. (1987) demonstrated that there was not a natural limiting process in the scale contraction of a surface front in an inviscid, non-hydrostatic high-resolution numerical simulation. Mudrick (1974), Shapiro (1975), Newton and Trevisan (1984), and Keyser and Pecnick (1985) simulated numerically the vertical circulations at upper-level fronts. The

results of these simulations are consistent with previous observations of fronts (e.g., Reed and Sanders 1953; Newton 1954; Bosart 1970).

Detailed observational studies of fronts are generally restricted to a single analysis of a limited portion of the front. As discussed by Keyser and Shapiro (1986), progress in understanding upper-level frontal dynamics has been hampered by the lack of spatial and temporal coverage in most case studies. Keyser and Shapiro (1986) also remark on the coupling between upper jet-front systems and lower tropospheric frontogenetical processes. Ideally, they should be studied as a unified phenomenon.

The OCEAN STORMS field experiment provided an opportunity to study different facets of one front in detail. OCEAN STORMS was an air-sea interaction experiment sponsored by the Office of Naval Research (ONR) in collaboration with the National Oceanic and Atmospheric Administration (NOAA); the National Weather Service (NWS); the Atmospheric Environment Service (AES) and the Institute of Ocean Sciences (IOS) from Canada; and U.S. and Canadian university scientists. NOAA P-3 research flights were conducted on 2 consecutive days within a single synoptic storm system, and in particular, the cold-front region of the storm. Because of the storm motion across the experimental domain, these flights were carried out in different regions of the storm system. The first flight on 9 December 1987 documented the structure of the cold front slightly downstream from a wind speed maximum of an upper-level jet. The second flight on 10 December 1987 was carried out in a region of moderate confluence in the entrance of the upper-level jet. Mesoscale analyses with a horizontal resolution of ~ 100 km were carried out from the surface to the upper troposphere for both flights. The distribution of ozone (O_3) on the second day was analyzed from flight-level data. In addition, microscale analyses (with a horizontal resolution of 200–1000 m) were carried out for the low-level portion of the front on the second day. Precipitation was absent in this region, and the front was accompanied by a narrow, shallow cumulus cloud line (rope cloud).

Fronts that have been analyzed previously on ~ 1 km scale or less have been either proximate to significant orography (e.g., Shapiro 1984; Colquhoun et al. 1985) or associated with significant precipitation (e.g., Browning and Harrold 1970; Carbone 1982; Hobbs and Persson

1982). In these cases, frontal scale contraction occurred through the combined effects of the adiabatic component of frontogenesis and either topographical influences or large spatial gradients in latent heating. The front studied here was free of these complicating effects, since it was nonprecipitating and over the ocean.

2. Flight Summary and Data Analysis

The research flight of 9 December was carried out within a mature synoptic-scale cyclone over the Gulf of Alaska. This flight was predominantly an Omega dropwindsonde (ODW) survey from ~400 mb; seven ODWs were deployed along a transect of the cold frontal zone from 48°N, 147°W to 43°N, 137°W.

The flight of 10 December included a comprehensive investigation of the cold front that was sampled only by ODWs the previous day. The flight had four stages; an ODW survey on the cold side of the front near 45°N, 130°W, a downward stairstep pattern heading south following the sloping frontal zone from ~500 mb to the boundary layer, a flight-level survey of the frontal structure within and near the top of the boundary layer in the vicinity of 38°N, 132°W, and ODW deployment on return to Seattle.

Our synoptic overview (Section 3) focuses on the environment within which the measurements of the cold front were taken. Sea-level pressure and frontal analyses were prepared from observations by buoys, ships of opportunity, coastal stations, and surface reports from the ODWs. Upper-air analyses were prepared from ODW and P-3 flight-level observations, and from rawinsonde soundings bordering the Gulf of Alaska and eastern North Pacific. The asynoptic aircraft observations were translated in space in a reference frame moving with the front using a two-dimensional Taylor's hypothesis.

Cross-section analyses were prepared for the front on 9 and 10 December. The analyses for 9 December were based upon ODWs released ~100 km apart during the transect of the cold front and on flight-level data averaged over 100 s (~10 km). The vertical resolution of the ODW data was ~100 m for temperature and humidity and ~700 m for wind velocity. The analyses for 10 December were based principally on flight-level data collected during the stairstep descent

through the frontal zone. The data were block averaged over 10 s intervals during ascents and descents, corresponding to a vertical resolution ranging between 50 and 100 m. Observations taken during horizontal flight segments were averaged over 100 s. Observations from two ODWs deployed shortly before the descent were incorporated into these analyses; data from ODWs deployed on the ferry leg back to Seattle (about 3 hours after the stairstep descent through the frontal zone) were used as a check on the flight-level data. For both data sets, a two-dimensional and steady-state assumption was made; all observations were projected onto vertical cross sections perpendicular to the front and in a frame of reference moving with the front. The propagation velocities of the front were estimated from satellite imagery. These observations were then used to construct cross-frontal distributions of wind velocity, thermodynamic structure and potential vorticity.

Microscale analyses of the leading edge of the front near the surface on 10 December were prepared from flight-level observations. Measurements from a series of transects of the front at an altitude of 600 m were averaged over 10 s (~1 km), and analyzed in a horizontal plane in a frame of reference moving with the front. Transects through the front at 1500, 900, and 600 m, were carried out before and after the 600 m horizontal survey. Observations collected during these flight legs were averaged over 2 s (~200 m) and plotted in a vertical cross section, perpendicular to and moving with the front. In this case the propagation velocity of the front was determined from its successive positions observed by the aircraft.

3. Synoptic Perspective

The synoptic perspective for this study was derived from sea-level pressure analyses at 0000 and 1200 UTC 9 December and 0000 UTC 10 December 1987; 850, 700, and 500 mb analyses at 0000 UTC 9 December and 0000 UTC 10 December 1987; and inclusive satellite imagery. Analyses at 0000 UTC on 9 and 10 December incorporated P-3 flight-level and ODW observations.

The sea-level pressure and frontal analyses, and ship and buoy observations for 0000 UTC 9 December (Fig. 1a) show a mature, 957 mb cyclone centered near 49°N, 147°W. Wind

direction shifts of ~ 60 degrees were present in the observed and geostrophic wind at the occluded and warm fronts, but weak wind direction shifts were present at the cold front. The cold front was propagating at southeastward $\sim 4 \text{ m s}^{-1}$, consistent with the observed front-normal wind component in the cold air. Significant weather occurred ahead of the occluded front near and to the north of the frontal triple point at 46°N , 132°W (Fig. 1a) where ships reported moderate to heavy rain and wind speeds up to 27 m s^{-1} . The 2346 UTC 8 December GOES-W infrared (IR) satellite image (Fig. 1b) shows the solid cloud shields associated with the fronts analyzed in Fig. 1a. The coldest (highest) cloud tops were at and ahead of the warm front and occluded front of the storm.

The 0000 UTC 9 December 850, 700, and 500 mb analyses (Figs. 2a-c) show strong temperature advectations and geostrophic wind shifts at the warm front near the Pacific Northwest coast. Cold-air advection was occurring at the cold front west of $\sim 147^\circ\text{W}$, but thermal advectations were minimal at the ODW transect of the cold front near 45°N , 142°W . There was weak warm-air advection on the anticyclonic side of the front at 500 mb (Fig. 2c). The 300 mb analysis from the U.S. National Meteorological Center (NMC) (not shown) indicated that the frontal transect was carried out slightly downstream from an upper-level jet streak. The intensity of this jet was $\sim 75 \text{ m s}^{-1}$ in the NMC analyses, but flight-level winds at 390 mb were as strong as 85 m s^{-1} . The occluded front and heavy weather shown in Fig. 1a were situated under the left exit region of this jet.

The sea-level pressure and frontal analyses for 1200 UTC 9 December (Fig. 3) show that the synoptic low center moved toward the northeast at $\sim 12 \text{ m s}^{-1}$ during the previous 12 hours with little change in central pressure. The warm front and occluded fronts were located along the Pacific Northwest coast. The wind direction shift at the cold front was still small north of about 40°N .

The sea-level pressure and frontal analyses for 0000 UTC 10 December (Fig. 4a) show westerly to northwesterly flow behind the cold front over most of the eastern North Pacific. The corresponding IR satellite image for 0046 UTC 10 December (Fig. 4b) shows that the cold front was two-dimensional in appearance west of 130°W . This image also shows that the solid cloud

deck accompanying the front did not extend into the upper troposphere. This was confirmed by ODW soundings in the vicinity of the cold front, which indicated cloud-top temperatures of -15°C . Precipitation was absent during low-level transects of the front south of 40°N .

The 0000 UTC 10 December geopotential and temperature analyses at 850, 700, and 500 mb (Figs. 5a–c) show cold-air advection at and behind the cold front extending southwestward from the Pacific Northwest coast. The 500 mb observations (Fig. 5c) suggest modest confluence and along-stream increases in wind speed west of $\sim 130^{\circ}\text{W}$. The maximum flight-level wind speed observed near the coast at $\sim 46^{\circ}\text{N}$, 128°W was $\sim 6\text{ m s}^{-1}$ greater than that measured near 43° , 134°W farther offshore along BB' (Fig. 5a).

The visible satellite imagery for ~ 1800 UTC 9 December through ~ 0000 UTC 10 December shows that the leading edge of the cold frontal cloud shield was accompanied by a narrow band of “bright” cumulus clouds south of $\sim 44^{\circ}\text{N}$. Seitter and Muench (1985) used the term “rope cloud” to describe a similar cloud feature at the leading edge of a cold front propagating over the Florida peninsula. They used data from an instrumented tower to show that the windshift associated with the rope cloud occurred over a horizontal scale of less than a few kilometers. Shapiro et al. (1985) found similar cloud lines associated with intense, microscale updrafts at the leading edge of frontal zones. Similar cloud structures of shorter length have been noted at the leading edge of thunderstorm outflows (Matthews 1981). A high-resolution visible image from a NOAA polar orbiting satellite at 2300 UTC 9 December (Fig. 6) provides a detailed view of a frontal rope cloud that resembles those discussed by Seitter and Muench (1985) and Shapiro et al. (1985). Figure 6 shows that the rope cloud undulated on a scale of ~ 200 km and that the reflectivity of the cloud elements that constitute the rope cloud varied on a scale of ~ 10 km.

4. Mesoscale Structure

Cross-section analyses of potential temperature (θ), along-frontal wind (u) and selected wind vectors for the front of 9 December (Fig. 7) show that the frontal zone was ~ 120 km wide near 400 mb, narrowing to less than 50 km near the surface. Above 700 mb, the cross-frontal

gradients in θ and u were $\sim 15 \text{ K (100 km)}^{-1}$ and $\sim 30 \text{ m s}^{-1} (100 \text{ km)}^{-1}$, respectively. The wind vectors show minimal directional change of the wind with height in the frontal zone. This is consistent with the constant-pressure analyses (Figs. 2a-c), which showed weak geostrophic thermal advections in the frontal zone. The axis of maximum u was found to be coincident with the warm (leading) edge of the frontal zone below $\sim 550 \text{ mb}$. Above this point, this axis was separate from the front within the warm air, resulting in a wedge of weaker cyclonic shear ahead of the front.

The analysis of the cross-frontal wind component (v) (Fig. 8) shows diffluence and possibly divergence within and to the warm side of the frontal zone above 3 km. A vertical shear in v of up to $\sim 20 \text{ m s}^{-1} (\text{km})^{-1}$ was also observed in this region. Given only a two-dimensional description, it is not possible to assess the degree of velocity divergence (convergence) or deformation. Similarly, it cannot be determined how much of the vertical shear in v is due to the along-frontal thermal gradient (geostrophic shear) versus the vertical shear in a transverse ageostrophic secondary circulation. The 500 mb geopotential and temperature analysis (Fig. 2c) shows a negative along-frontal thermal gradient (geostrophic warm-air advection) to the south of the frontal zone, but it is too weak to account for the observed magnitude of the vertical shear.

The relative humidity (RH) analysis (Fig. 9) shows that the air was very dry ($\text{RH} < 10\%$) in the upper portion of the frontal zone. The RH in the frontal zone was less than 50% down to $\sim 2 \text{ km}$. The RH was greater than 90% throughout the remainder of the cross section.

The spatial resolution of our measurements and analyses permitted reasonable estimates of the distribution of cross-frontal isentropic potential vorticity (IPV). Our technique consisted first of an analysis of absolute momentum (Eliassen 1962),

$$m = u - fy, \quad (1)$$

where f is the Coriolis parameter and y is the cross-front coordinate, increasing toward colder air. As reviewed by Keyser and Shapiro (1986), in situations of two-dimensionality, IPV can be expressed as

$$\text{IPV} = J_{yp}(m, \theta) = \frac{\partial m}{\partial y_p} \frac{\partial \theta}{\partial p} - \frac{\partial m}{\partial p} \frac{\partial \theta}{\partial y_p} \quad (2)$$

where p is pressure. The magnitude of IPV is inversely proportional to the area of the solenoids formed by the intersections of m and θ isopleths. The distribution of m and θ (Fig. 10a), and the corresponding distribution of IPV (Fig. 10b) show that IPV of a magnitude greater than $2 \times 10^{-5} \text{ K mb}^{-1} \text{ s}^{-1}$ extended down the frontal zone to near 800 mb. Intermediate values of IPV (Fig. 10b) and RH (Fig. 9) were found for the wedge of air between the frontal zone and the axis of maximum along-frontal wind speed above ~ 550 mb. Similar IPV distributions were shown in earlier studies (e.g., Reed 1955; Reed and Danielson 1959, Shapiro 1978).

Cross-section analyses were constructed for the front sampled on 10 December using flight-level measurements, which have a better resolution than ODW observations. Figure 11 shows the distribution of θ and u in a cross section normal to the front using the same vertical and horizontal scales used for the analyses of 9 December (Figs. 7–10). It is apparent that the front had a shallower slope on 10 December (Fig. 11) than on 9 December (Fig. 7). Mid-tropospheric (2–4 km) differences in θ and u across the frontal zone were comparable to those observed on 9 December. Since the frontal zone was wider on 10 December, horizontal gradients were about 50% to 70% of their counterparts of the day before. Above ~ 2 km, the magnitude of the along-frontal wind speed was $\sim 8 \text{ m s}^{-1}$ less than that on 9 December.

The distribution of v on 10 December (Fig. 12) shows that cross-frontal flow was directed mostly toward colder air and lower geopotential heights, and confluence in v was found within the frontal zone from the surface up to ~ 500 mb. In contrast, the v analysis for 9 December (Fig. 8) showed diffluence above ~ 700 mb and generally flow toward warmer air and higher heights. A significant fraction of the vertical shear in v on 10 December can be attributed to the

along-frontal temperature gradient; the 700 mb analysis (Fig. 5b) yields a geostrophic vertical shear in the cross-frontal wind of $\sim 3 \text{ m s}^{-1} (100 \text{ mb})^{-1}$.

RH within the frontal zone above $\sim 600 \text{ mb}$ was less than 10% on both 9 and 10 December, but there were some differences between the RH distributions. Figure 13 shows that on 10 December the RH was greater than 90% only within the boundary layer and within a plume extending up to $\sim 550 \text{ mb}$ along the warm side of the front. On 9 December the RH was greater than 90% everywhere except within the frontal zone down to $\sim 700 \text{ mb}$ (Fig. 9).

The distribution of m and θ (Fig. 14a) and IPV (Fig. 14b) for 10 December shows an intrusion of stratospheric IPV extending to below 700 mb within the frontal zone. As would be expected, the degree of tropopause folding was less than that shown for 9 December (Fig. 10b), since the cross section on 9 December was in the vicinity of the wind speed maximum where the upper-level front was near its maximum strength.

The O_3 analysis (Fig. 15) for 10 December shows an intrusion of stratospheric O_3 extending from the warm side of the front at 5 km down to its cold side near the surface. The maximum concentrations of O_3 were found $\sim 50 \text{ km}$ to the warm side of the maximum values in IPV near 500 mb. The separation between these maxima decreased closer to the surface and was non-existent at $\sim 700 \text{ mb}$. The O_3 signature of tropopause folding extended farther down to lower altitudes than the IPV signature.

5. Microscale Structure: 10 December

This section describes the microscale structure of the lower portion of the front shown in Figs. 11–15. This represents the first microscale documentation of a nonprecipitating cold front and associated rope cloud over the ocean.

Microscale cross-section analyses of θ and u and selected wind vectors (Fig. 16) were constructed from horizontal transects across the front at 600, 900, and 1500 m.* The difference

* The most critical step in this part of the analysis was the alignment of the separate flight legs, since space-time adjustments based on the mean frontal propagation speed were not sufficiently accurate for a microscale analysis. The procedure used was to identify the main frontal updraft plume from the frontal penetrations at 600 and

(continued...)

in θ across the front was only ~ 1 K near the surface, but the horizontal shear in u was substantial ($\sim 6 \text{ m s}^{-1}$ over 500 m). The u analysis shows that the frontal "head" extended up to ~ 1000 m. The lowest frontal transect was at 600 m, at about the height of the frontal zone behind the elevated head.

Figure 17 shows relative flow vectors in the cross-frontal plane and an analysis of equivalent potential temperature (θ_e). The primary frontal updraft was ~ 1 km wide and reached a peak of 5 m s^{-1} . The upward motion decreased rapidly with height between 900 and 1500 m. Descent was observed ~ 1 km behind and ahead of the main updraft. Apparently the majority of the convergence in the cross-frontal wind associated with the updraft occurred below 600 m; the corresponding divergence aloft appears to have occurred mostly between 900 and 1500 m. The average magnitude of the updraft ($\sim 3 \text{ m s}^{-1}$) at 600 m corresponds to an average convergence of $\sim 5 \times 10^{-3} \text{ s}^{-1}$ over a width of 1 km. The isotachs of the along-frontal wind (Fig. 16) are nearly parallel to the relative flow vectors, suggesting that this quantity was approximately conserved in the low-level portion of the frontal zone. The θ_e analysis shows a frontal head up to ~ 1000 m, and that the thermodynamic gradients in the lower portion of the frontal zone were concentrated on a horizontal scale of less than 1 km.

Seitter and Muench (1985) found excellent agreement between the observed propagation speed of a rope cloud and the speed predicted by a gravity current model. Smith and Reeder (1988) and Moncrieff (1989) discuss the application of gravity current models to low-level fronts. Within the denser fluid, there is a region of relative flow from rear to front in the classic, laboratory version of a gravity current. We observed a small region of relative flow toward the front behind the elevated head, but our observations were not close enough to the surface to compare with a gravity current model. Seitter and Muench (1985) suggested that their rope cloud

*(...continued)

900 m and to assume that they were aligned vertically. This provided a local estimate of the frontal propagation speed which was then used to displace the 1500 m transect. The frontal transects were made about 7 minutes apart. Bond and Fleagle (1985) assumed that the frontal updraft was oriented vertically in a microscale analysis of a cold front using P-3 flight-level data; this assumption is also consistent with the aircraft observations of a front by Shapiro et al. (1985) and the results of the Doppler radar studies of cold fronts by Browning and Harrold (1970) and Hobbs and Persson (1982).

was propagating ahead of the normal surface frontal position due to an outflow of evaporatively cooled air below the frontal surface. In the present case, the rope cloud and the leading edge of the front were continuous with the frontal zone above the boundary layer.

Previous detailed frontal case studies (with the exception of the Doppler-radar-based studies) have been limited to a single two-dimensional snapshot of the front. These studies have not assessed the nature and magnitude of temporal and along-frontal variability. For the present study a series of horizontal transects across the front were flown at 600 m. An isotach analysis and selected wind vectors along the flight track (Fig. 18) show a narrow (<1 km) zone of horizontal cyclonic shear vorticity at the front. As shown in the vertical cross sections (Figs. 16–17), thermodynamic gradients were concentrated within the same shear zone. A prominent lateral displacement between linear segments of the front is shown near the central portion of Fig. 18. During the north-south transect in the vicinity of this displacement, the main updraft was relatively weak. The front was stronger at the east-west transect near the same location. Separate analyses of the along-frontal and cross-frontal wind components (not shown), as defined by the mesoscale orientation of the front, indicate that the divergence in the along-frontal component compensated for much of the convergence in the cross-frontal component in the vicinity of the lateral displacement. The thermodynamic data suggested that another along-frontal perturbation was present near the east-west transect shown in the left half of Fig. 18.

James and Browning (1979) and Hobbs and Persson (1982) used ground-based Doppler radars to analyze narrow cold-frontal rainbands. They found that strong surface fronts were composed of a series of “line elements” or “precipitation cores” of enhanced frontal characteristics 20–30 km in length separated by “gap regions” of weaker frontal characteristics 5–10 km in length. The frontal zone represents a maximum in vorticity and would therefore be subject to a shear instability by Rayleigh’s criterion; this instability is suggested in the present case in the absence of precipitation and large variations in latent heating. Unfortunately, our observations were not sufficient to determine a wavelength for along-frontal perturbations. The single gap region that was well observed here had a length of ~3 km.

Additional variations in frontal structure can be seen in high resolution (~200 m) data from 600 and 900 m altitude transects of the front. Figure 19 shows four sets of traces of θ , u , vertical velocity (w), and pressure perturbation (p') from the 600-m transects of the front, plotted in a frame of reference normal to the mean mesoscale orientation of the front and moving with its mean propagation velocity. Simultaneous measurements of pressure and radar altitude were used to estimate the pressure along the flight track at the mean height of the track; p' was calculated as the difference between the height-adjusted pressure and the mean pressure along the track. The first two transects (aa' and bb') encountered a narrow (<1 km), well-defined frontal zone, as indicated by the frontal ascent plume and the change in the along-frontal wind (Figs. 19a,b). In both cases p' was relatively high at the leading (warm) edge of the ascent plume and frontal zone, and relatively low at the trailing (cold) edge of the frontal zone. The magnitude of the pressure difference was ~ 0.8 mb. Similar structures (not shown) were found in other transects of well-defined portions of the front. The intensity of frontal gradients generally decreased toward the southwest.

The third and fourth traces (Figs. 19c,d) shown are for the north-south (cc') and east-west (dd') transects of the front, respectively, in the vicinity of the lateral displacement of the front shown in central portion of Fig. 18. The north-south transect (Fig. 19c) encountered relatively weak frontal gradients.* The p' signature encountered during transects of well-defined portions of the front (e.g., as shown in Figs. 19a,b) was absent. The frontal zone at the east-west transect near the offset (Fig. 19d) was well-defined with respect to the frontal updraft and the shear in the along-frontal wind, but a p' signal was lacking. Evidently, this reflects the proximity of this transect to the lateral displacement in the front.

Observations from 900 m transects through well-defined portions of the front are shown in Figs. 20a,b. In each case, the most prominent p' feature was a ~ 0.5 mb minimum at the trailing (cold) portion of the updraft.

* The projection used for Fig. 19c was based on the mean mesoscale orientation of the front, which yields an exaggerated horizontal scale for this transect. Since the updraft was weaker, as well as broader, the front was apparently less intense here.

Similar pressure perturbation patterns for the strong, precipitating cold front studied by Carbone (1982) were derived from Doppler radar data through a retrieval method (Gal-Chen 1978) by Parsons et al. (1987). Figure 6 from Parsons et al. (1987) shows that a pressure perturbation maximum was present below the main frontal updraft and that a ridge of high pressure extended to the leading (warm) edge of the updraft near 2 km. Perturbation lows were found near 3 km behind the main updraft. Based on the depth of the cold air behind the front, our transects at 600 and 900 m are roughly equivalent to the 2 and 3 km levels for their case. The location, sense, and magnitude of the pressure perturbations measured directly here correspond with those calculated indirectly by Parsons et al. (1987). It is perhaps surprising that the pressure perturbations for the two cases are of comparable magnitude, since the Parsons et al. (1987) front was substantially stronger. This agreement can be attributed to a matter of scale; partly because kinematic gradients in the frontal zones were comparable, and also because their analysis had a ~1 km horizontal resolution and more smoothing than our analysis with a ~200 m resolution.

Parsons et al. (1987) found considerable along-frontal variations in wind and pressure, and our results are consistent with the results from their study. In particular, their Fig. 12a shows that the pressure perturbation was weak in the region of a localized vortex associated with a wave along the front with a wavelength of 13 km. This vortex was situated in a region of lateral displacement between linear segments of the front (as shown by the radar reflectivity in their Fig. 3). Our observations are less complete, but as shown in Figs. 19c,d, a significant pressure perturbation was also absent near a similar feature along our front.

6. Discussion

Research aircraft observations have been used to describe mesoscale frontal structure slightly downstream from a wind speed maximum of an upper-level jet and in a region of moderate confluence upstream of the same wind speed maximum. In both regions, a tropopause fold extended down to 800–700 mb (2–3 km above the surface), as revealed by analyses of IPV

and O_3 . The tropopause folding was more extreme in the vicinity of the speed maximum, where the upper-level front was stronger.

The analyses for the second day (10 December) showed that the cross-frontal confluence and cyclonic shear occurred in the presence of positive along-frontal thermal gradients (cold-air advection). Shapiro (1981) and Keyser and Pecnick (1985), among others, showed that this condition favored the development of strong upper fronts. Their results showed that the frontogenesis due to confluence was enhanced by tilting associated with a shift of the transverse ageostrophic circulation toward the warm side of the jet. Our observations were not sufficient to calculate the transverse ageostrophic circulation for this case. Indirect evidence, namely the analyses of the cross-frontal wind component (Fig. 12), relative humidity (Fig. 13), and O_3 (Fig. 15), suggest that downward motion was concentrated within the frontal zone above ~ 600 mb. Our results are therefore consistent with the observed and modeled upper-tropospheric jet configurations reviewed by Keyser and Shapiro (1986).

Most earlier observational studies have examined upper-level fronts or surface fronts as physically and dynamically distinct entities. There are important dynamical differences; e.g., tilting can be an important frontogenetical effect at upper fronts but is generally frontolytical near the surface. Even though the frontogenetical mechanisms may have varied with height, in the present case, the result was a structurally continuous frontal zone spanning the entire troposphere. This is consistent with our observations of enhanced concentrations of O_3 within the frontal zone from near 500 mb down to the boundary layer (Fig. 15). Some earlier studies (e.g., Reed 1955, and Palmén 1958) include examples of fronts spanning the troposphere.

The microscale observations and analyses of the front revealed a narrow (<1 km) zone of wind direction shift and strong updraft at the leading edge of the front. The θ_e analysis (Fig. 17) showed an elevated frontal head; similar structures have been observed by Shapiro et al. (1985) at nonprecipitating cold fronts accompanied by rope clouds. The microscale analyses also revealed significant along-front variability in the form of a lateral displacement between linear segments of the front. Quasi-periodic structures of a similar nature have been observed

by Doppler radar (e.g., James and Browning 1979; Carbone 1982; Hobbs and Persson 1982) at precipitating fronts.

Organized horizontal wavelike perturbations along frontal zones have been presumed to be associated with horizontal shear instabilities (e.g., Hobbs and Persson 1982); however this issue has received limited theoretical attention. Haurwitz (1949) examined the stability of a simple case of a shear zone of finite width and found that the most unstable perturbation along the shear zone had a wavelength ~ 8 times the width of the shear zone. The growth rate of this instability is rapid; the e-folding time would be ~ 10 min for the front studied here. His stability analysis showed a short-wave cutoff but only a slow decrease in growth for waves longer than the most unstable. Moore (1985) carried out a stability analysis for a frontal zone with cyclonic shear and unstable stratification; he found that the most unstable waves had properties similar to those observed by radar. The frontal zone in the present case was convectively neutral ($\delta\theta_e/\delta z \sim 0$); the shear in the along-frontal component was evidently sufficient to generate the along-front perturbations. Linear stability results should be applied to a vigorous surface front with caution. Boundary layer air flows continually into the vigorous updraft at the leading edge of the front and parcels have typical residence times of only hundreds of seconds within the low-level frontal zone, yet radar studies (e.g., Hobbs and Persson 1982) have tracked individual along-frontal perturbations for a few hours. These perturbations must be maintained by some type of feedback mechanism or mechanisms that act on the air that is being ingested into the frontal zone.

Future frontal research should be aimed at advancing our understanding of the structure and theory of along-frontal variability under both quasi-adiabatic and strongly diabatic conditions. Even the mean structure of fronts may be influenced by along-frontal variations, through the effects of these variations on the vertical circulations at fronts. Another fruitful area of future research concerns the transition from hydrostatic to non-hydrostatic dynamics in the scale contraction of fronts, including modifications due to diabatic and viscous effects.

Acknowledgments. The authors acknowledge the NOAA Office of Aircraft Operations for providing the P-3 research aircraft used in this study. Financial support for the authors was provided by the Office of Naval Research (ONR). Additional support for NAB was provided by the Fisheries Oceanography Coordinated Investigation (FOCI). Dave Parsons and Brad Smull provided constructive criticisms of a draft of this manuscript. The technical support staff at the NOAA Pacific Marine Environmental Laboratory helped prepare the manuscript. Contribution 1162 from NOAA Pacific Marine Environmental Laboratory.

Chapman, J.R., D.J. Stensrud, C.B. Chelton, R.K. Smith and K. McInnes, 1985: The convective layer of stratocumulus Australia: A synoptically forced cold front. *Mon. Wea. Rev.*, 113, 2040-2107.

Ekman, A., 1959: On the formation of fronts in the atmosphere. *The Atmosphere and the Sea in Motion*, B. Bolin, Ed., Rockefeller Inst. Press, New York, 277-287.

Ekman, A., 1962: On the vertical circulation in frontal zones. *Geophys. Publ.*, 34, 147-160.

Gal-Chen, T., 1978: A method for the initialization of the anvil-convective cloud system for nesting models with observations. *Mon. Wea. Rev.*, 106, 507-508.

Gal, P.L., R.T. Williams and T.L. Clark, 1987: On the mid-range scale of surface fronts. *J. Atmos. Sci.*, 44, 2562-2574.

Haurwitz, K., 1949: The instability of wind discontinuities and their origin in planetary circulations. *J. Meteor.*, 8, 200-205.

Hobbs, P.V., and P.O.G. Parmesan, 1972: The mesoscale and synoptic-scale structure and organization of clouds and precipitation in midlatitude regions: Part V: The relationship of mesoscale cold-frontal rainbands. *J. Atmos. Sci.*, 29, 280-295.

Hoskins, B.J., and P.P. Marshall, 1975: Atmospheric mesoscale structure: Mathematical representation and solution. *J. Atmos. Sci.*, 32, 11-37.

Lin, C., T.C. Chen, A. Arkin, and D. Kuyper, 1984: Numerical simulation of frontogenesis in a convective atmosphere. *J. Atmos. Sci.*, 41, 2581-2594.

REFERENCES

- Bond, N.A., and R.G. Fleagle, 1985: Structure of a cold front over the ocean. *Quart. J. Roy. Meteor. Soc.*, **111**, 739–759.
- Bosart, L.F., 1970: Mid-tropospheric frontogenesis. *Quart. J. Roy. Meteor. Soc.*, **96**, 442–471.
- Browning, K.A., and T.W. Harrold, 1970: Air motion and precipitation at a cold front. *Quart. J. Roy. Meteor. Soc.*, **96**, 369–389.
- Carbone, R.E., 1982: A severe winter squall line. Stormwide hydrodynamic structure. *J. Atmos. Sci.*, **39**, 258–279.
- Colquhoun, J.R., D.J. Shepherd, C.E. Coulman, R.K. Smith and K. McInnes, 1985: The southerly buster of southeastern Australia: An orographically forced cold front. *Mon. Wea. Rev.*, **113**, 2090–2107.
- Eliassen, A., 1959: On the formation of fronts in the atmosphere. *The Atmosphere and the Sea in Motion*, B. Bolin, Ed., Rockefeller Inst. Press, New York, 277–287.
- Eliassen, A., 1962: On the vertical circulation in frontal zones. *Geophys. Publ.*, **24**, 147–160.
- Gal-Chen, T., 1978: A method for the initialization of the anelastic equations: Implications for matching models with observations. *Mon. Wea. Rev.*, **106**, 587–606.
- Gall, R.L., R.T. Williams and T.L. Clark, 1987: On the minimum scale of surface fronts. *J. Atmos. Sci.*, **44**, 2562–2574.
- Haurwitz, B., 1949: The instability of wind discontinuities and shear zones in planetary atmospheres. *J. Meteor.*, **6**, 200–206.
- Hobbs, P.V., and P.O.G. Persson, 1982: The mesoscale and microscale structure and organization of clouds and precipitation in midlatitude cyclones. Part V: The substructure of narrow cold-frontal rainbands. *J. Atmos. Sci.*, **39**, 280–295.
- Hoskins, B.J., and F.P. Bretherton, 1972: Atmospheric frontogenesis models: Mathematical formulation and solution. *J. Atmos. Sci.*, **29**, 11–37.
- Hsie, E.-Y., R.A. Anthes and D. Keyser, 1984: Numerical simulation of frontogenesis in a moist atmosphere. *J. Atmos. Sci.*, **41**, 2581–2594.

- James, P.K., and K.A. Browning, 1979: Mesoscale structure of line convection at surface cold fronts. *Quart. J. Roy. Meteor. Soc.*, **105**, 371–382.
- Keyser, D., and R.A. Anthes, 1982: The influence of planetary boundary layer physics on frontal structure in the Hoskins-Bretherton horizontal shear model. *J. Atmos. Sci.*, **39**, 1783–1802.
- Keyser, D., and M.J. Pecnick, 1985: A two-dimensional primitive equation model of frontogenesis forced by confluence and horizontal shear. *J. Atmos. Sci.*, **42**, 1259–1282.
- Keyser, D., and M.A. Shapiro, 1986: A review of the structure and dynamics of upper-level frontal zones. *Mon. Wea. Rev.*, **114**, 452–499.
- Larsen, M.F., and J. Röttger, 1982: VHF and UHF Doppler radars as tools for synoptic research. *Bull. Amer. Meteor. Soc.*, **63**, 996–1008.
- Matthews, D.A., 1981: Observation of a cloud arc triggered by thunderstorm outflow. *Mon. Wea. Rev.*, **109**, 2140–2157.
- Moncrieff, M.W., 1989: Analytical models of narrow cold-frontal rainbands and related phenomena. *J. Atmos. Sci.*, **46**, 150–162.
- Moore, G.W.K., 1985: The organization of convection in the narrow cold-frontal rainband. *J. Atmos. Sci.*, **42**, 1777–1791.
- Mudrick, S.E., 1974: A numerical study of frontogenesis. *J. Atmos. Sci.*, **31**, 869–892.
- Neiman, P.J., P. May, M.A. Shapiro and B. Stankov: Radioacoustic sounding system observations of an arctic front. *Mon. Wea. Rev.*, (submitted 1990).
- Newton, C.W., 1954: Frontogenesis and frontolysis as a three-dimensional process. *J. Meteor.*, **11**, 449–461.
- Newton, C.W., and A. Trevisan, 1984: Clinogenesis and frontogenesis in jet-stream waves. Part II: Channel model numerical experiments. *J. Atmos. Sci.*, **41**, 2735–2755.
- Palmén, E., 1958: Vertical circulation and release of kinetic energy during the development of Hurricane Hazel into an extratropical storm. *Tellus*, **10**, 1–23.
- Parsons, D.B., C.G. Mohr, and T. Gal-Chen, 1987: A severe frontal rainband. Part III: Derived thermodynamic structure. *J. Atmos. Sci.*, **44**, 1615–1631.

- Reed, R.J., 1955: A study of a characteristic type of upper-level frontogenesis. *J. Meteor.*, **12**, 226–237.
- Reed, R.J., and F. Sanders, 1953: An investigation of the development of a mid-tropospheric frontal zone and its associated vorticity field. *J. Meteor.*, **10**, 338–349.
- Reed, R.J., and E.F. Danielsen, 1959: Fronts in the vicinity of the tropopause. *Arch. Meteor. Geophys. Bioklim.*, **A11**, 1–17.
- Sawyer, J.S., 1956: The vertical circulation at meteorological fronts and its relation to frontogenesis. *Proc. Roy. Soc. London*, **A234**, 346–362.
- Seitter, K.L., and H.S. Muench, 1985: Observation of a cold front with a rope cloud. *Mon. Wea. Rev.*, **113**, 840–848.
- Shapiro, M.A., 1974: A multiple structured frontal zone-jet stream system as revealed by meteorologically instrumented aircraft. *Mon. Wea. Rev.*, **102**, 244–253.
- Shapiro, M.A., 1975: Simulation of upper-level frontogenesis with a 20-level isentropic coordinate primitive equation model. *Mon. Wea. Rev.*, **103**, 591–604.
- Shapiro, M.A., 1978: Further evidence of the mesoscale and turbulent structure of upper level jet stream-frontal zone systems. *Mon. Wea. Rev.*, **106**, 1100–1111.
- Shapiro, M.A., 1980: Turbulent mixing within tropopause folds as a mechanism for the exchange of chemical constituents between the stratosphere and troposphere. *J. Atmos. Sci.*, **37**, 994–1004.
- Shapiro, M.A., 1981: Frontogenesis and geostrophically forced secondary circulations in the vicinity of jet stream-frontal zone systems. *J. Atmos. Sci.*, **38**, 954–973.
- Shapiro, M.A., 1984: Meteorological tower measurements of a surface cold front. *Mon. Wea. Rev.*, **112**, 1634–1639.
- Shapiro, M.A., T. Hampel, and D.W. van de Kamp, 1984: Radar wind profiler observations of fronts and jet streams. *Mon. Wea. Rev.*, **112**, 1263–1266.
- Shapiro, M.A., T. Hampel, D. Rotzoll and F. Moses, 1985: The frontal hydraulic head: A micro-scale (1 km) triggering mechanism for mesoconvective weather systems. *Mon. Wea. Rev.*, **113**, 1166–1185.

Smith, R.K., and M.J. Reeder, 1988: On the movement and low-level structure of cold fronts.

Mon. Wea. Rev., **116**, 1927-1944.

Williams, R.T., 1974: Numerical simulation of steady-state fronts. *J. Atmos. Sci.*, **31**, 1286-1296.

Williams, R.T., R.C. Chou and C.J. Cornelius, 1981: Effects of condensation and surface motion on the structure of steady-state fronts. *J. Atmos. Sci.*, **38**, 2365-2376.

Figure Captions

Fig. 1a. Sea-level pressure and frontal analysis for 0000 UTC 9 December 1987. Ship, buoy and coastal observations include air temperature ($^{\circ}\text{C}$), wind vectors (one full barb = 5 m s^{-1}), and sea-level pressure (mb) plotted using the standard convention.

Fig. 1b. GOES-W IR satellite image for 2346 UTC 8 December.

Fig. 2a. 850 mb height (solid lines, 3 dam interval) and temperature (dashed contours, 2°C interval) for 0000 UTC 9 December. AA' is the cross-section projection line for Figs. 7–10.

Fig. 2b. As in Fig. 2a, but for 700 mb.

Fig. 2c. As in Fig. 2a, but for 500 mb. Note that the height is contoured at an interval of 6 dam.

Fig. 3. As in Fig. 1a, but for 1200 UTC 9 December.

Fig. 4a. As in Fig. 1a, but for 0000 UTC 10 December.

Fig. 4b. GOES-W IR satellite image for 0046 UTC 10 December.

Fig. 5a. 850 mb height (solid lines, 3 dam interval) and temperature (dashed contours, 2°C interval) for 0000 UTC 10 December. BB' is the cross-section projection line for Figs. 11–15.

Fig. 5b. As in Fig. 5a, but for 700 mb.

Fig. 5c. As in Fig. 5a, but for 500 mb. Note that the height is contoured at an interval of 6 dam.

Fig. 6. NOAA Polar Orbiter visible satellite image for 2300 UTC 9 December.

Fig. 7. Cross-section analyses of potential temperature (K, solid lines) and along-frontal (from 245°) component of the wind (m s^{-1} , dashed lines) valid at 0000 UTC 9 December along the cross-section projection line AA' of Fig. 2a. Heavy solid lines signify the boundaries of the frontal zone. Selected wind reports are also plotted. The dots and wind reports show the locations of the ODW observations; the release times of the ODWs are indicated at the bottom.

Fig. 8. Cross-section analysis of the cross-frontal (from 335°) component of the wind (m s^{-1}), as in Fig. 7, in a frame of reference moving with the front. The arrows indicate wind direction.

Fig. 9. Cross-section analysis of relative humidity (%), as in Fig. 7.

Fig. 10. Cross-section analysis of (a) absolute momentum (m s^{-1} , solid lines) and potential temperature (K, dashed lines) and (b) potential vorticity ($10^{-5} \text{ K mb}^{-1} \text{ s}^{-1}$), as in Fig. 7.

Fig. 11. Cross-section analyses of potential temperature (K, solid lines) and along-frontal (from 237°) component of the wind (m s^{-1} , dashed lines) valid at 0000 UTC 10 December along the cross-section projection line BB' of Fig. 5a. Heavy solid lines signify the boundaries of the frontal zone. Selected wind reports are also plotted. The dots and wind reports show the locations of the flight-level and ODW observations.

Fig. 12. Cross-section analysis of the cross-frontal (from 327°) component of the wind (m s^{-1}), as in Fig. 11, in a frame of reference moving with the front. The arrows indicate wind direction.

Fig. 13. Cross-section analysis of relative humidity (%), as in Fig. 11.

Fig. 14. Cross-section analysis of (a) absolute momentum (m s^{-1} , solid lines) and potential temperature (K, dashed lines) and (b) potential vorticity ($10^{-5} \text{ K mb}^{-1} \text{ s}^{-1}$), as in Fig. 11.

Fig. 15. Cross-section analysis of ozone (pphm vol^{-1}), as in Fig. 11. Solid lines refer to whole units of pphm vol^{-1} , dashed lines are intermediate contours.

Fig. 16. Cross-section analyses of potential temperature (K, solid lines) and along-frontal (from 237°) component of the wind (m s^{-1} , dashed lines) based on P-3 flight data taken between 0315 and 0333 UTC 10 December. Selected elected wind reports are also plotted. The dots and wind reports show the locations of the observations.

Fig. 17. Cross-section analysis of equivalent potential temperature (K, solid lines) and vectors of motion relative to the front, as in Fig. 16. The vector scaling is shown in the lower right-hand corner.

Fig. 18. Isotachs (m s^{-1}) and selected wind barbs at 600 m from P-3 flight data collected between 0305 and 0410 UTC 10 December. Flight data were averaged over 10 s

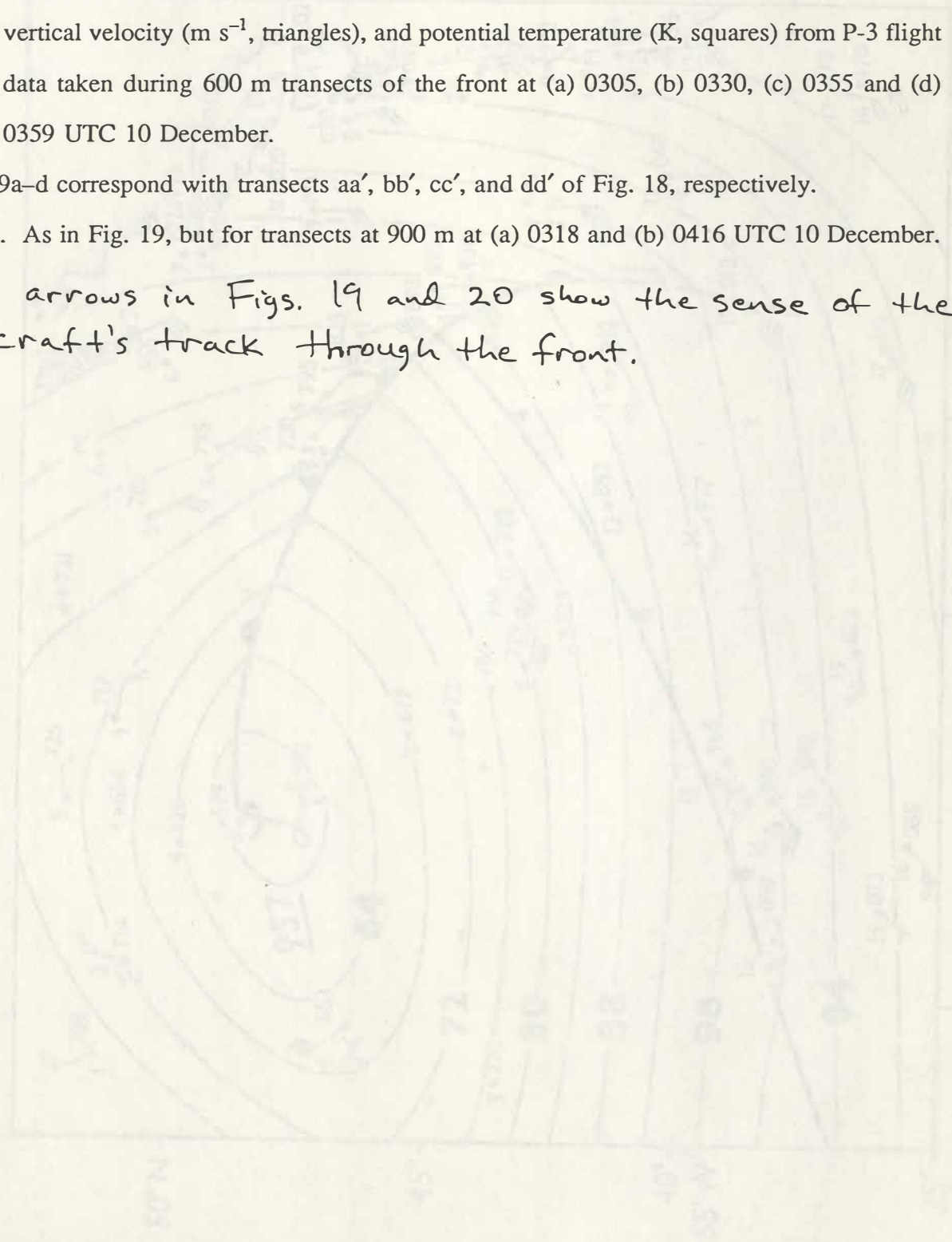
(equivalent to a horizontal resolution of ~ 1 km) and plotted in a frame of reference moving with the front. The dotted line is the flight track.

Fig. 19. Pressure perturbation (mb, solid lines), along-frontal wind speed (m s^{-1} , open circles), vertical velocity (m s^{-1} , triangles), and potential temperature (K, squares) from P-3 flight data taken during 600 m transects of the front at (a) 0305, (b) 0330, (c) 0355 and (d) 0359 UTC 10 December.

Figs. 19a–d correspond with transects aa', bb', cc', and dd' of Fig. 18, respectively.

Fig. 20. As in Fig. 19, but for transects at 900 m at (a) 0318 and (b) 0416 UTC 10 December.

The arrows in Figs. 19 and 20 show the sense of the aircraft's track through the front.



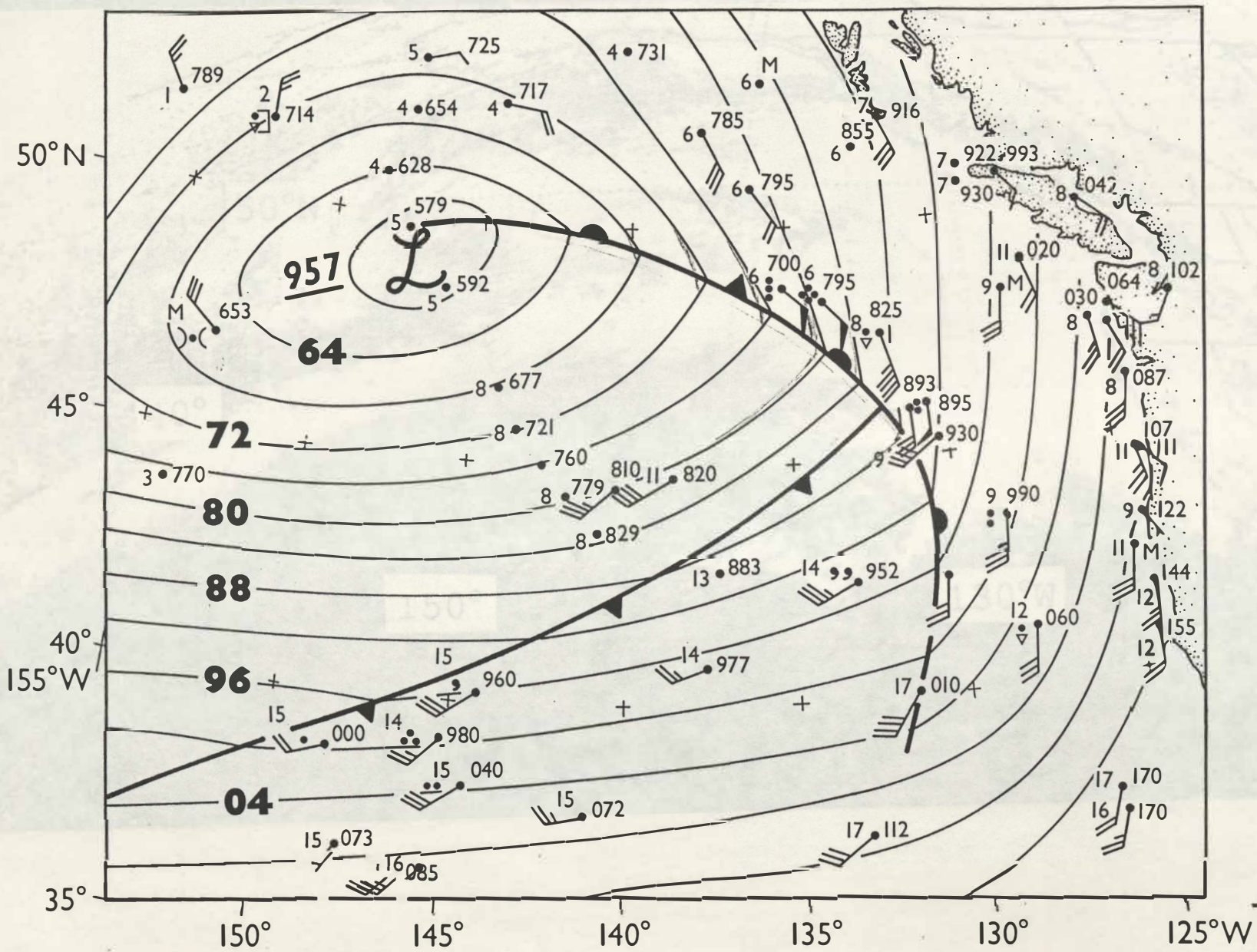


Fig. 1a

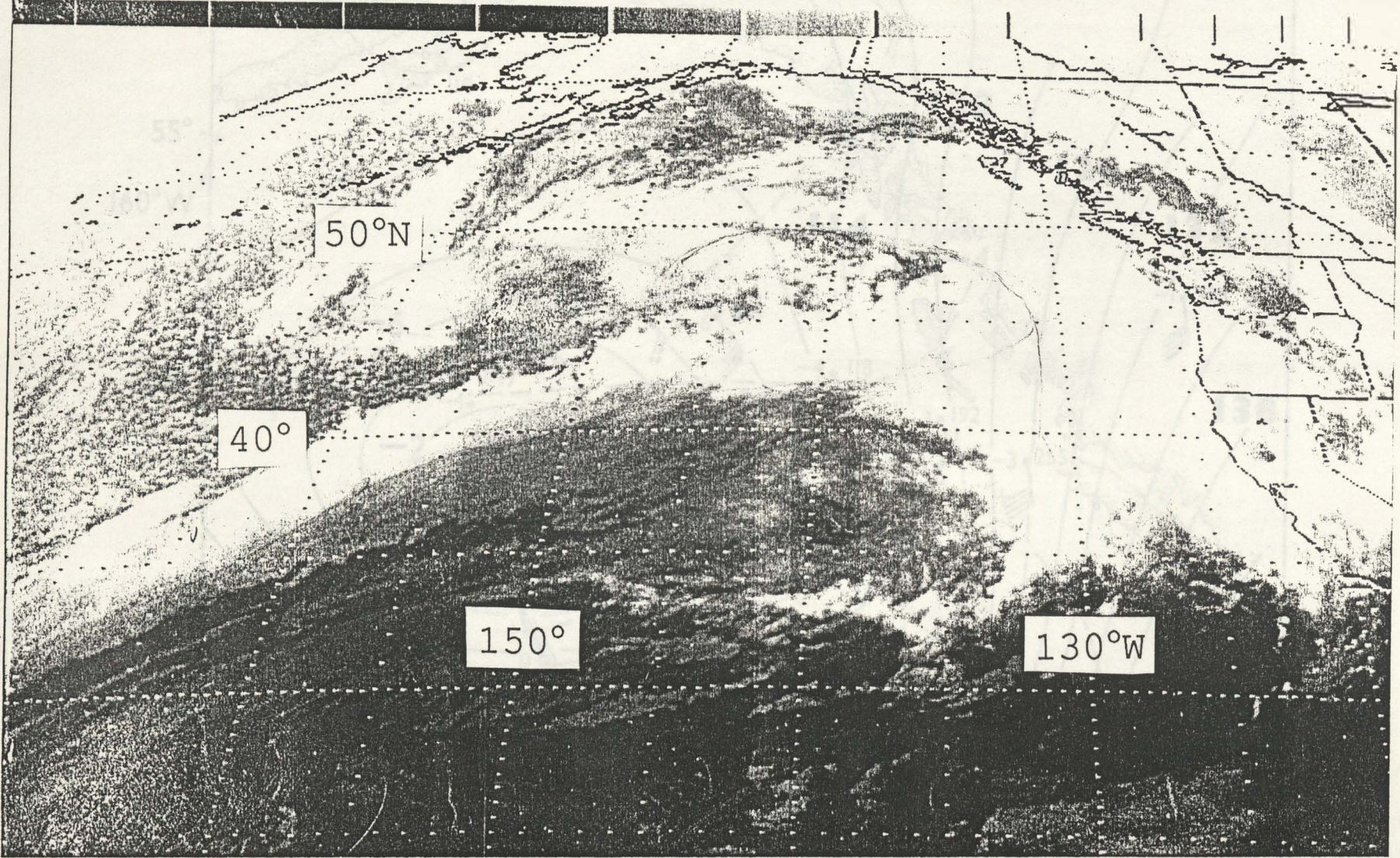


Fig. 1b

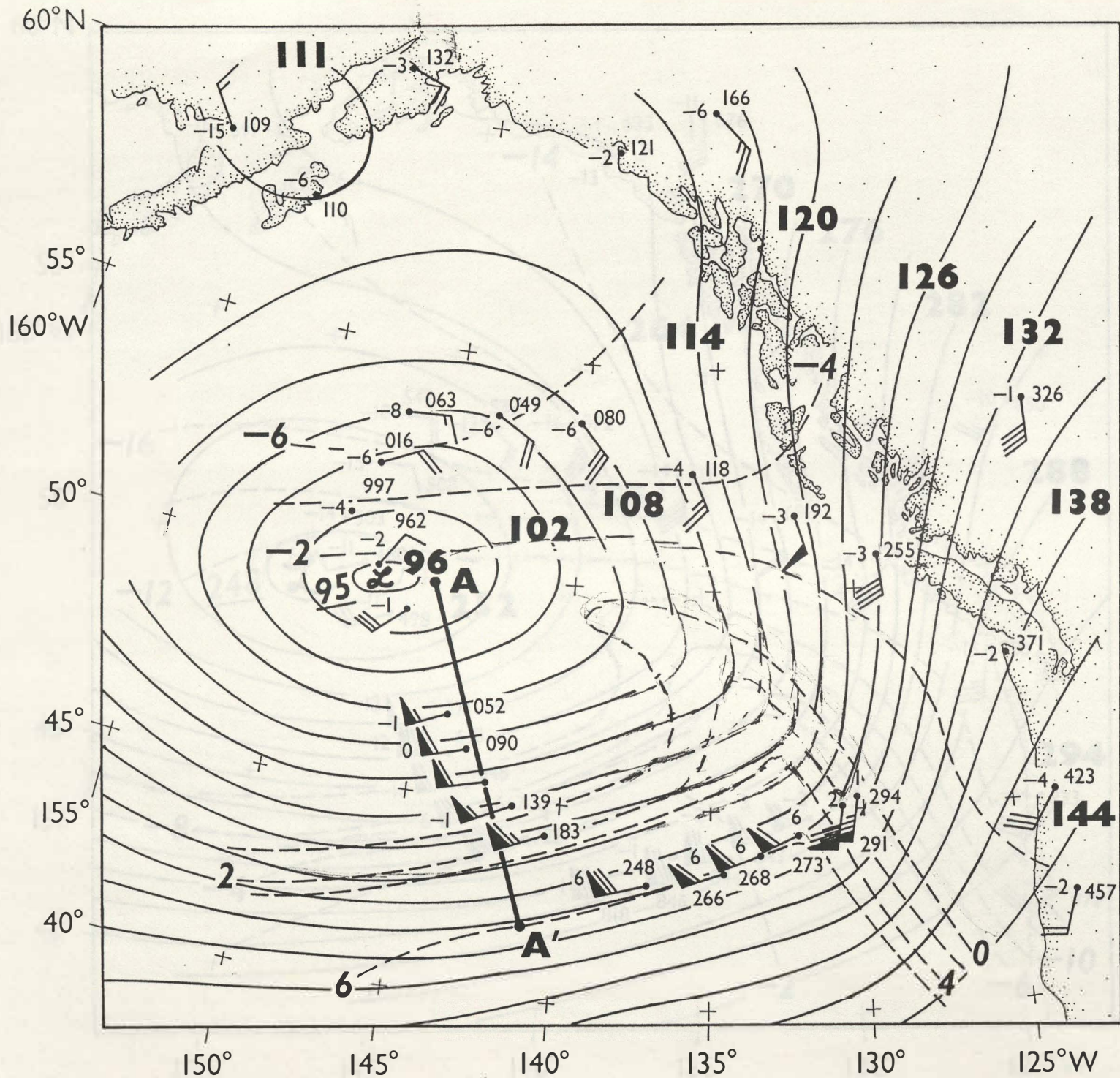


Fig. 2a

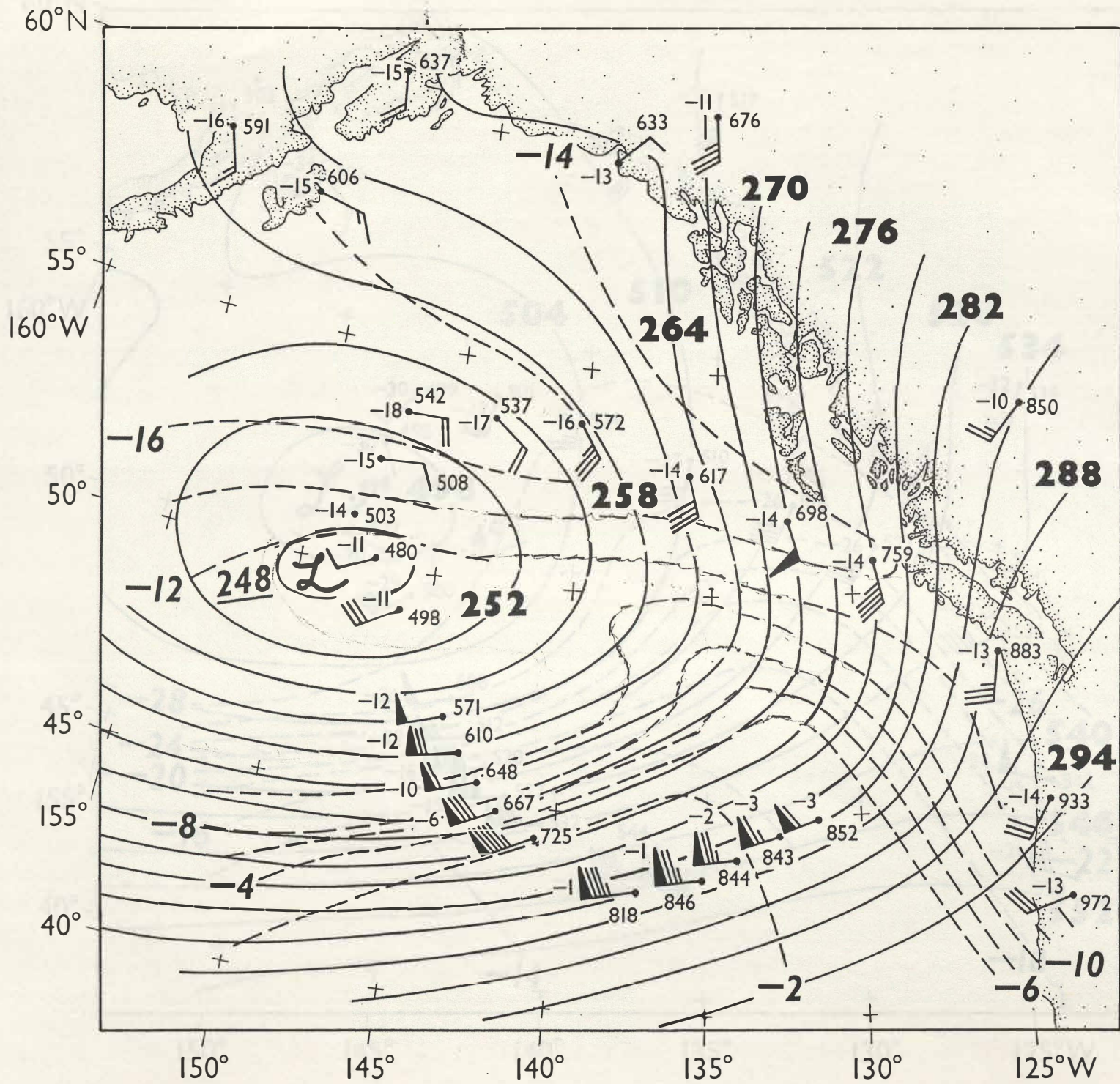


Fig. 26

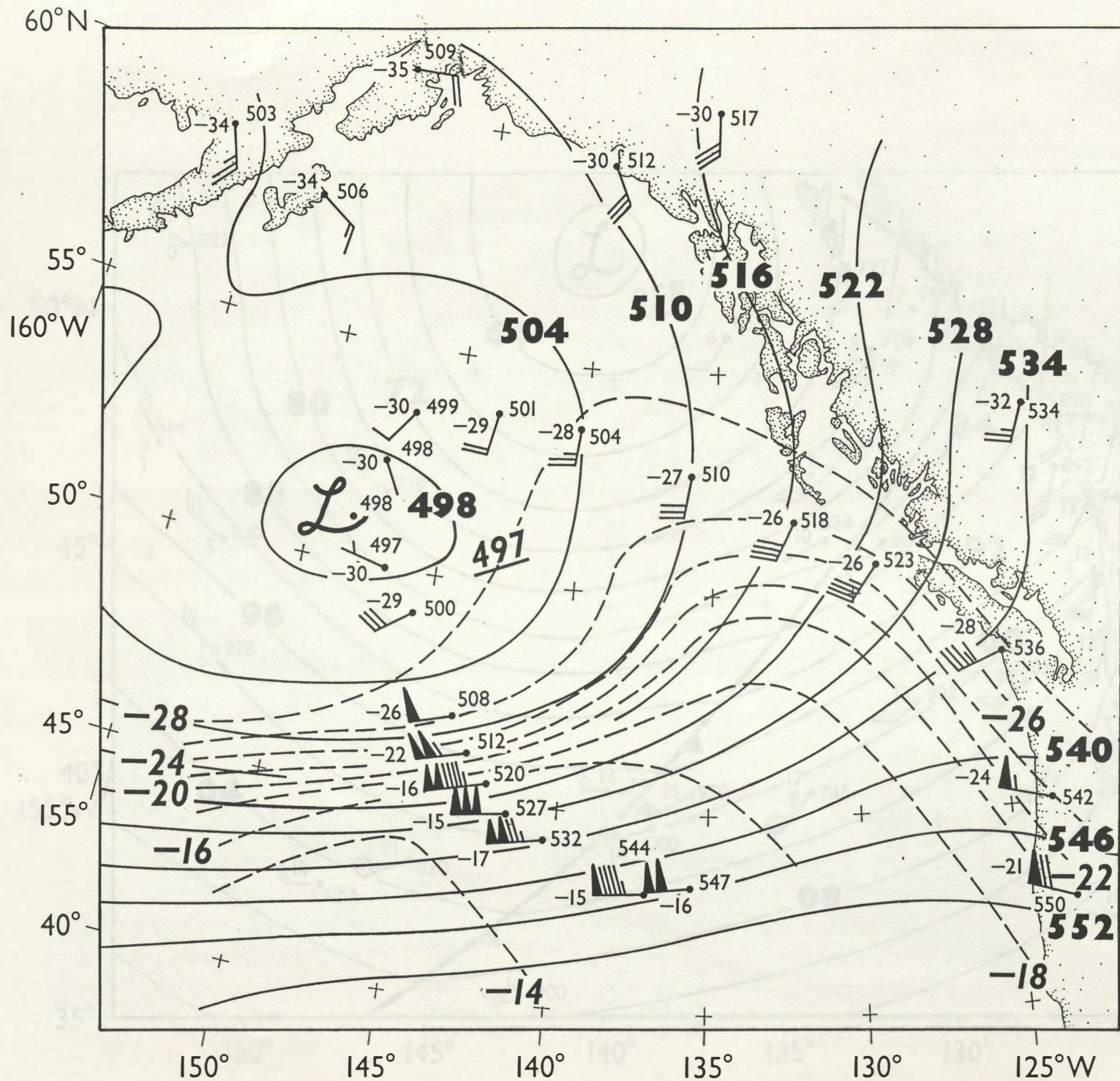


Fig. 2c

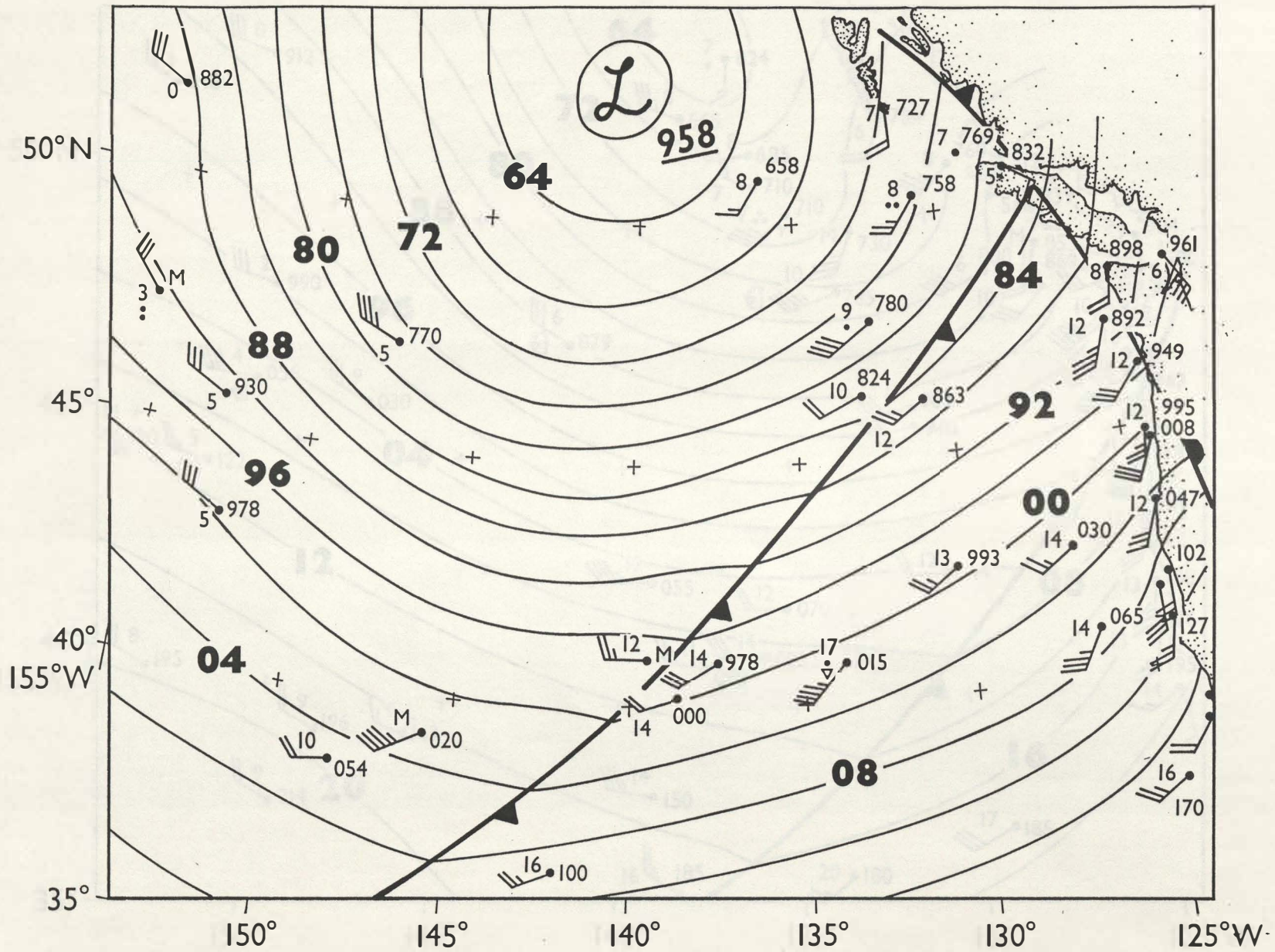


Fig. 3

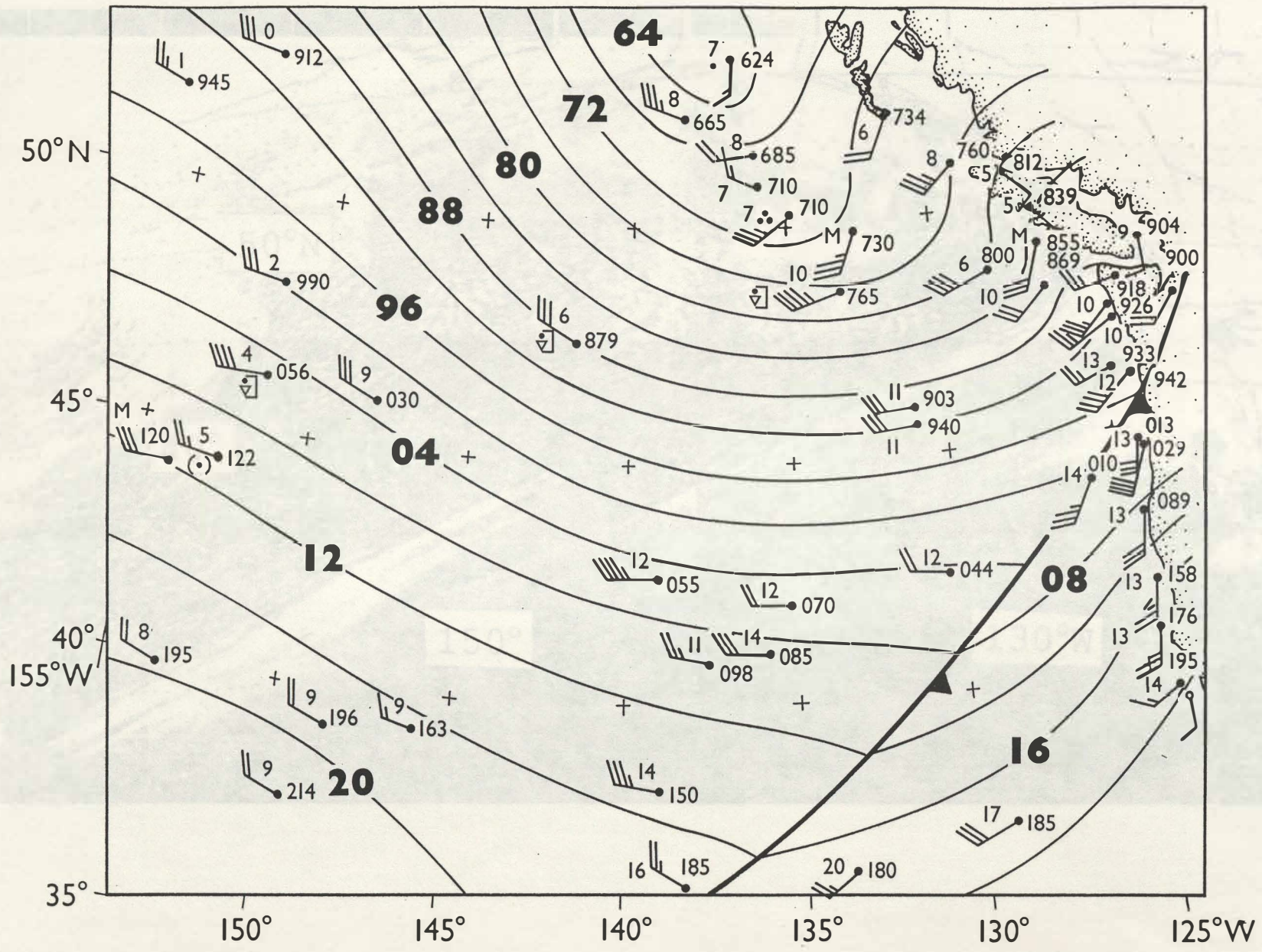


Fig. 4a

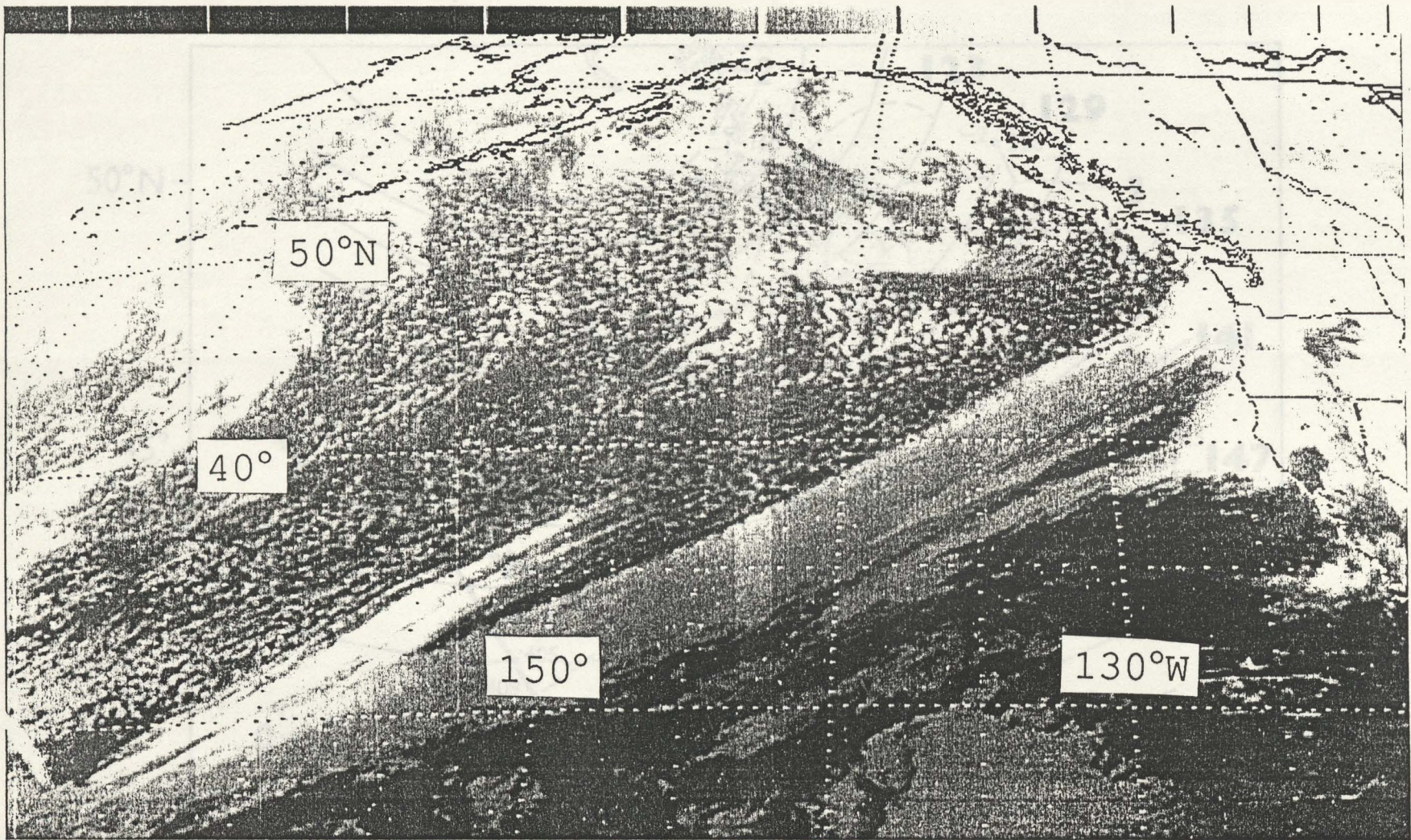


Fig. 46

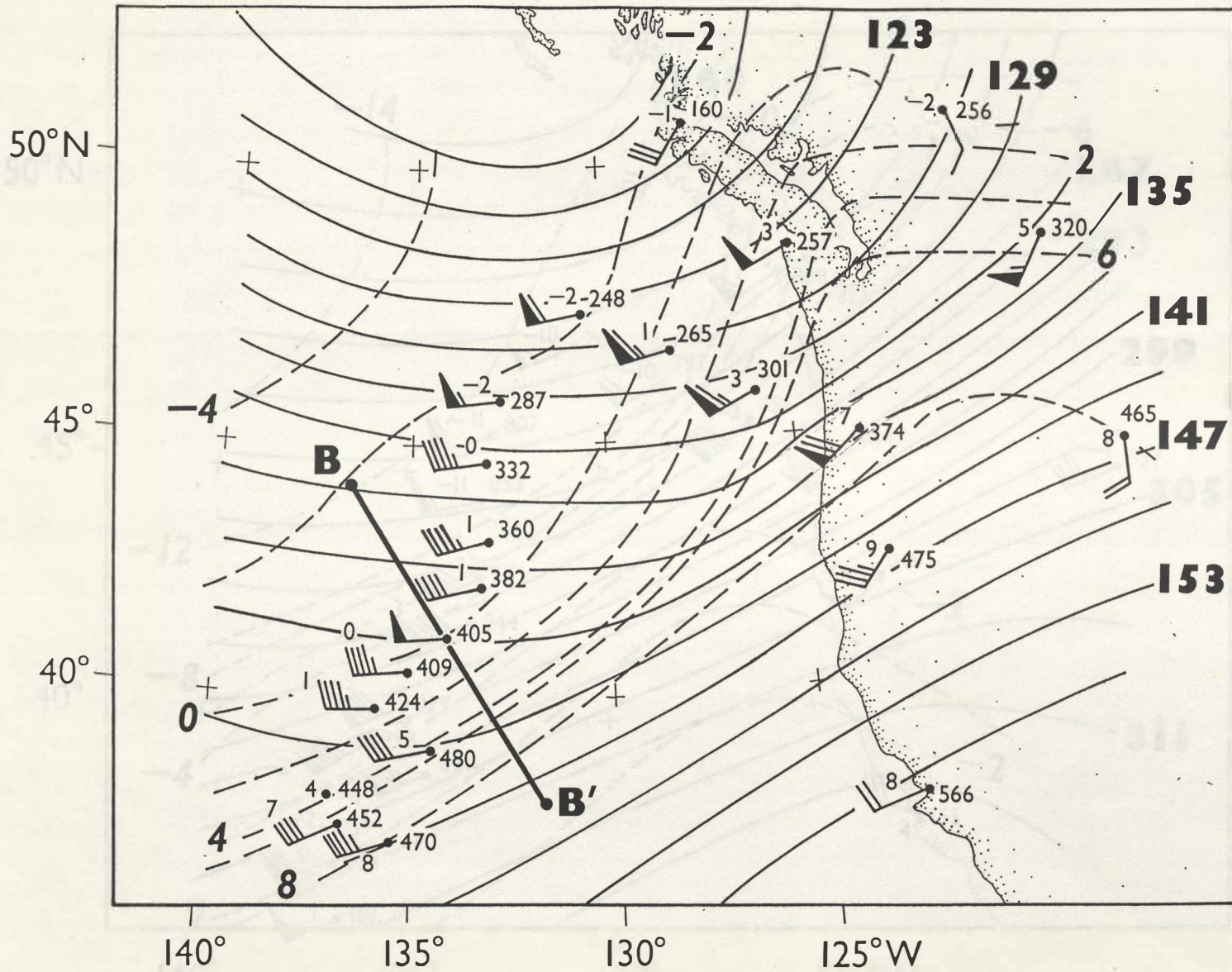


Fig. 5a

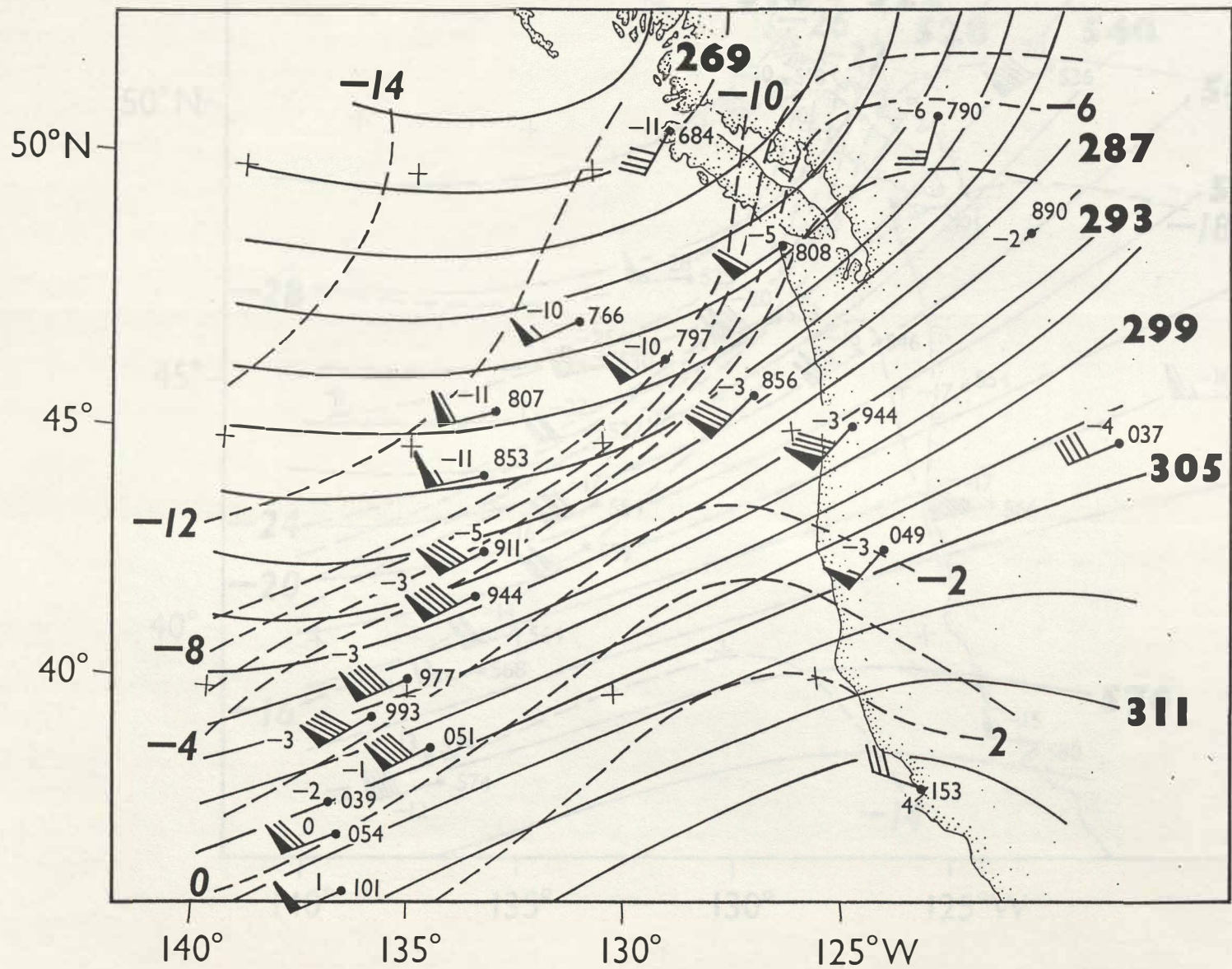


Fig. 516

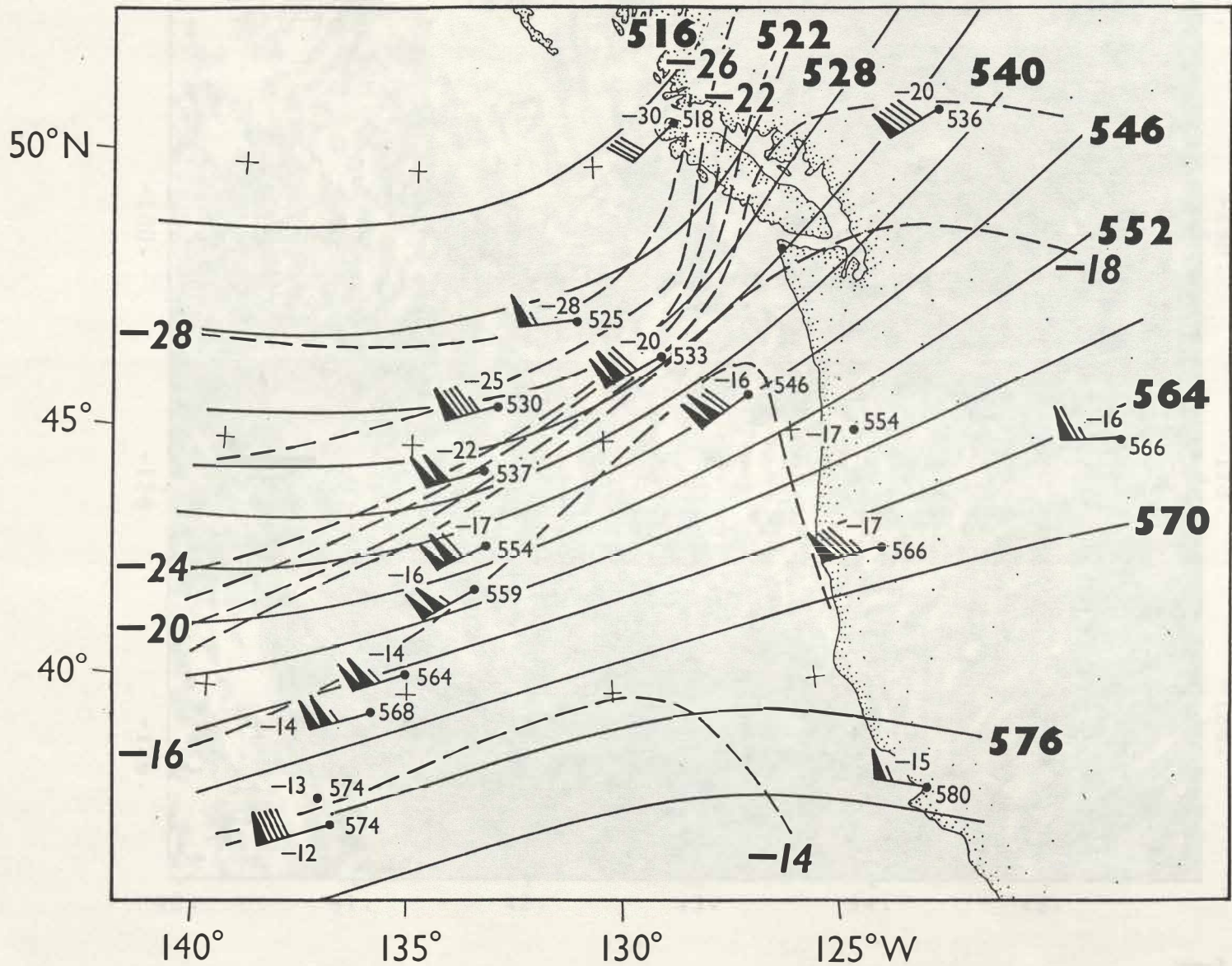


Fig. 5c

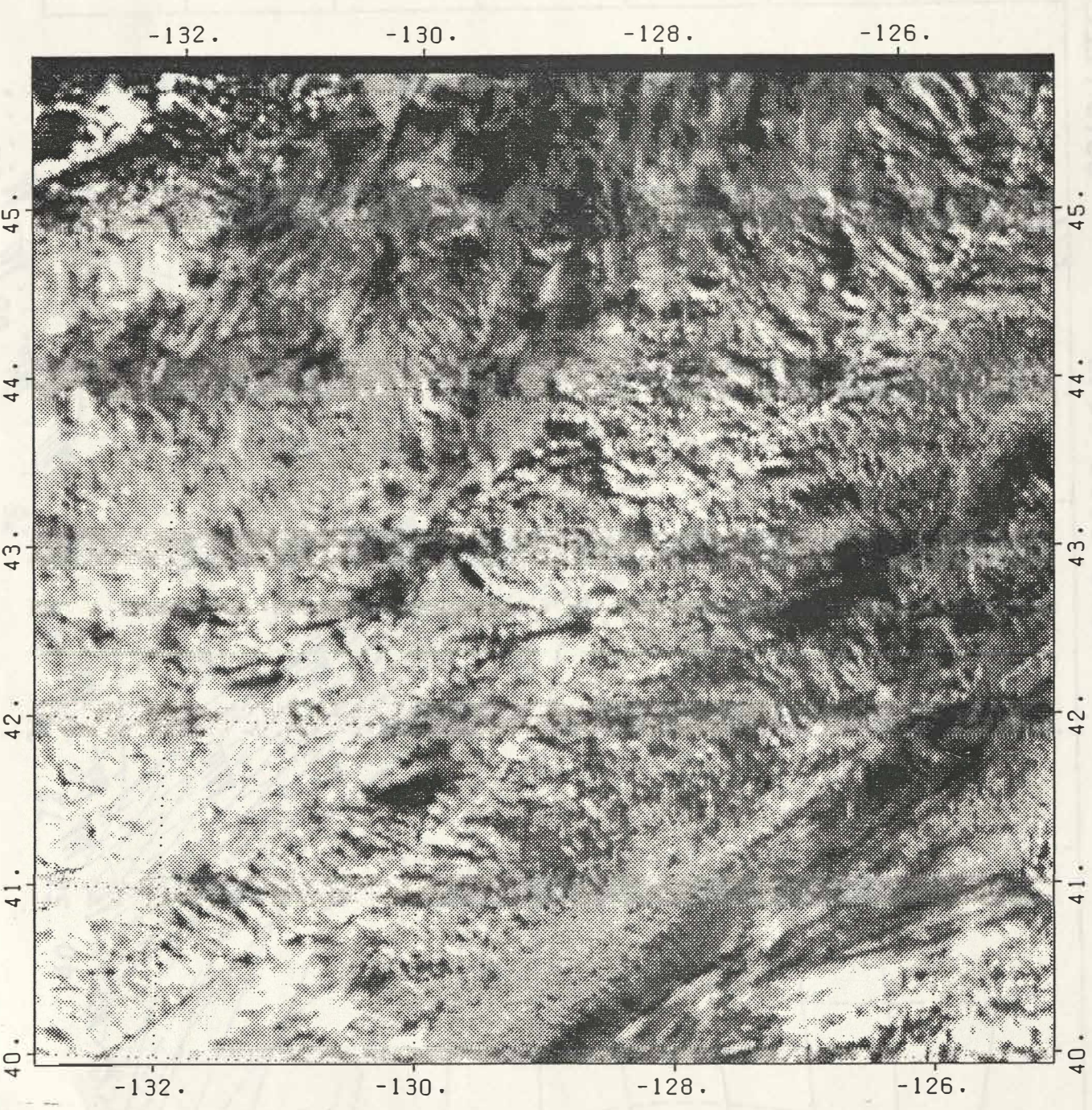


Fig.6

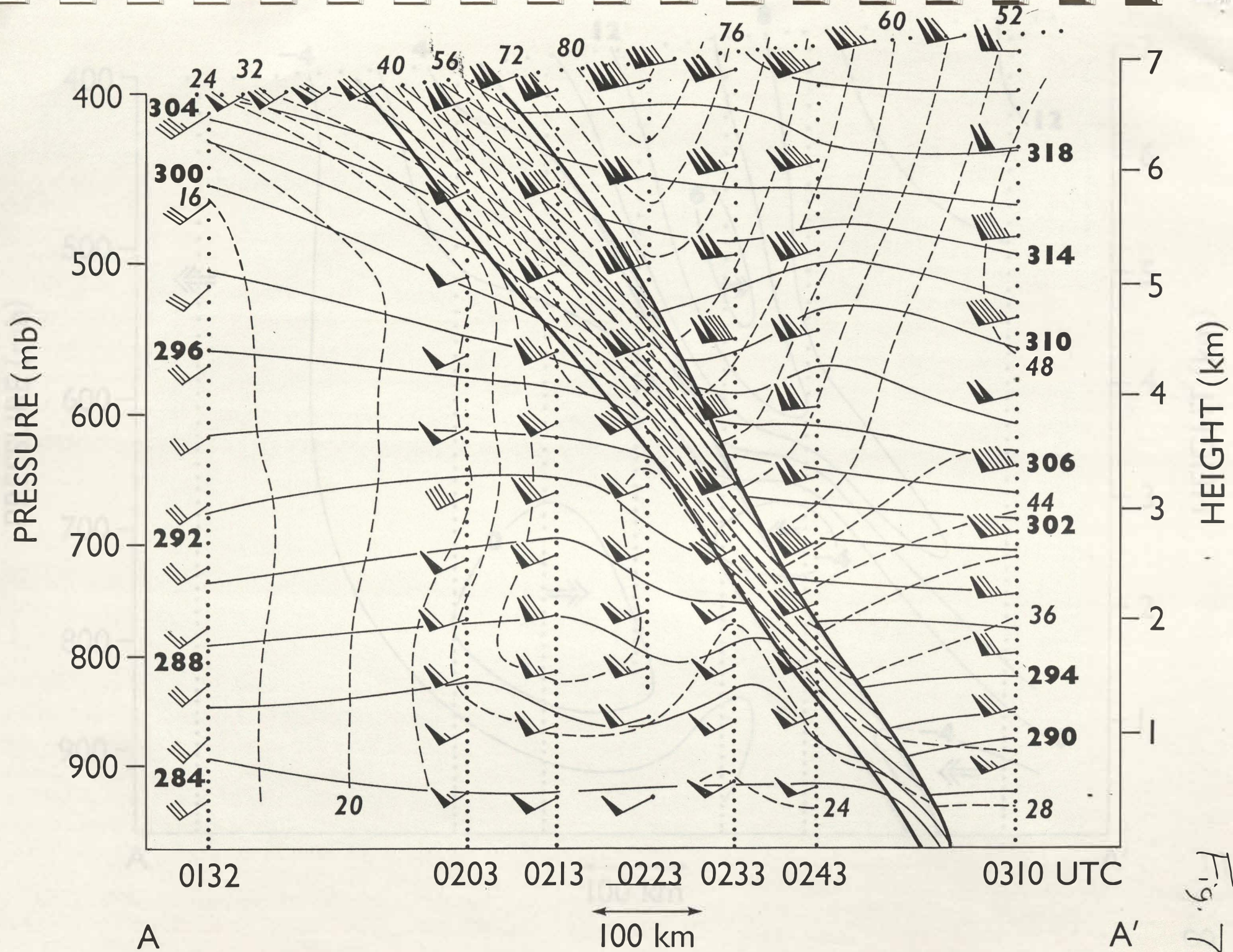


Fig. 7

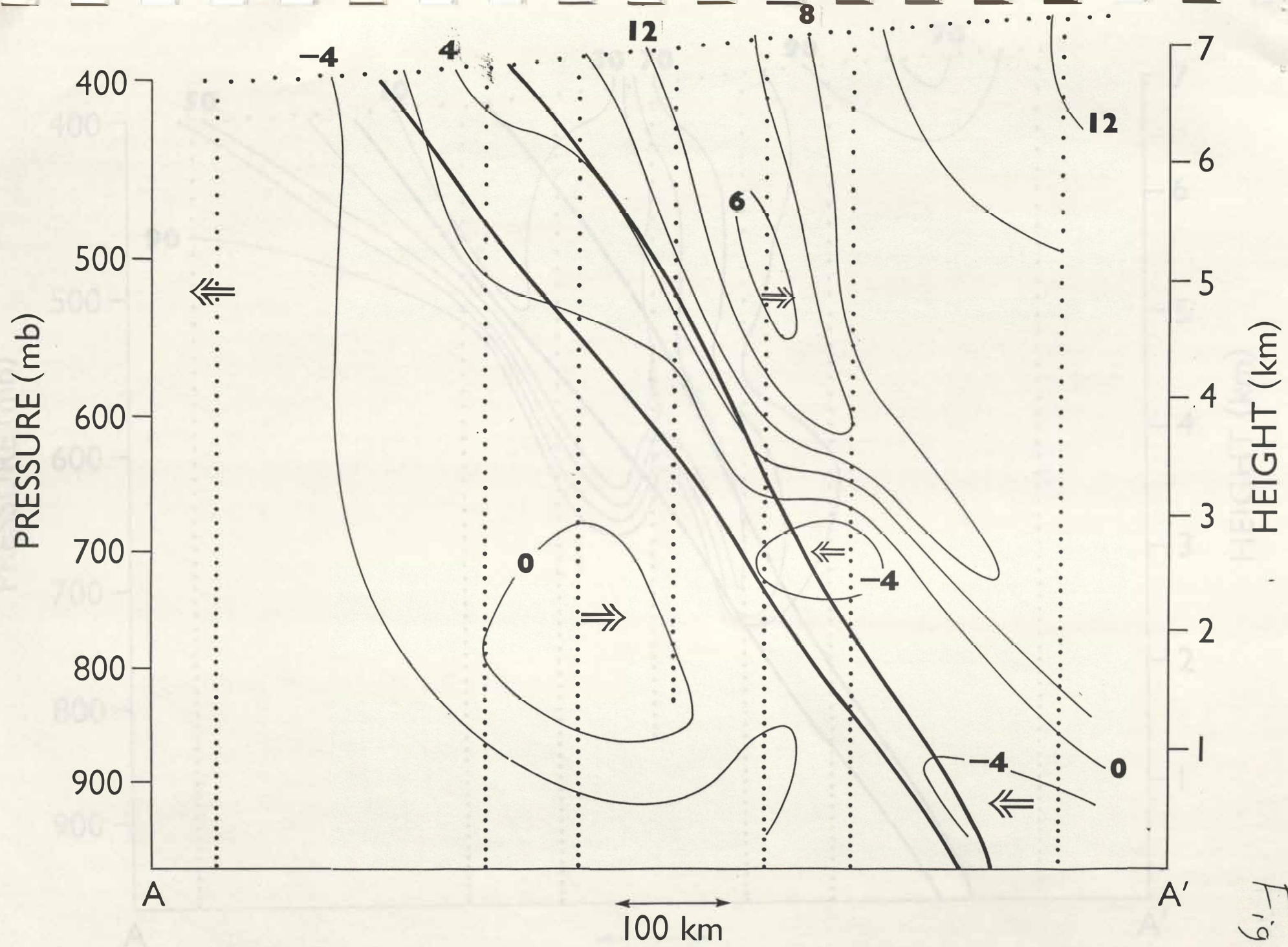


Fig. 8

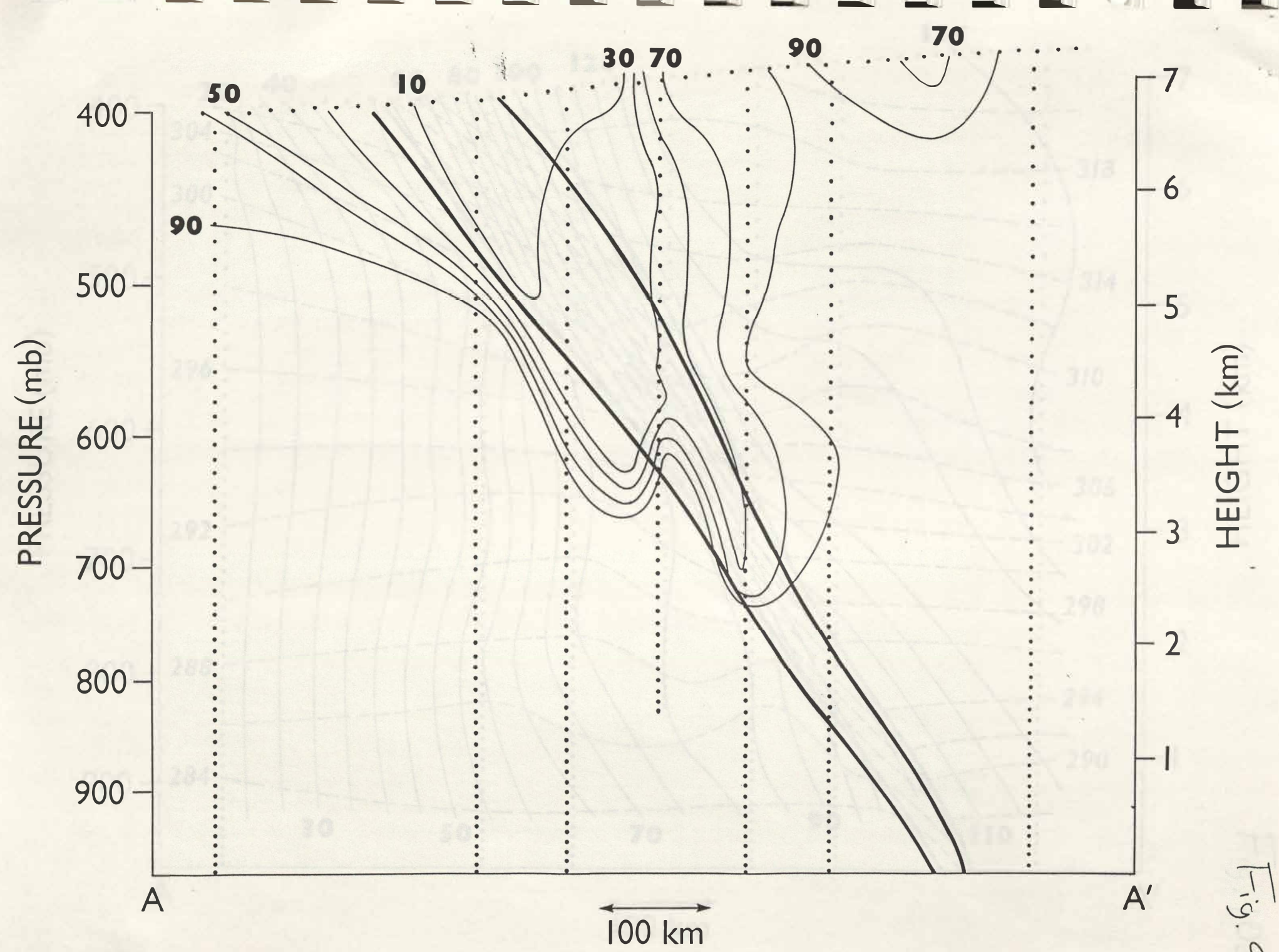


Fig. 9

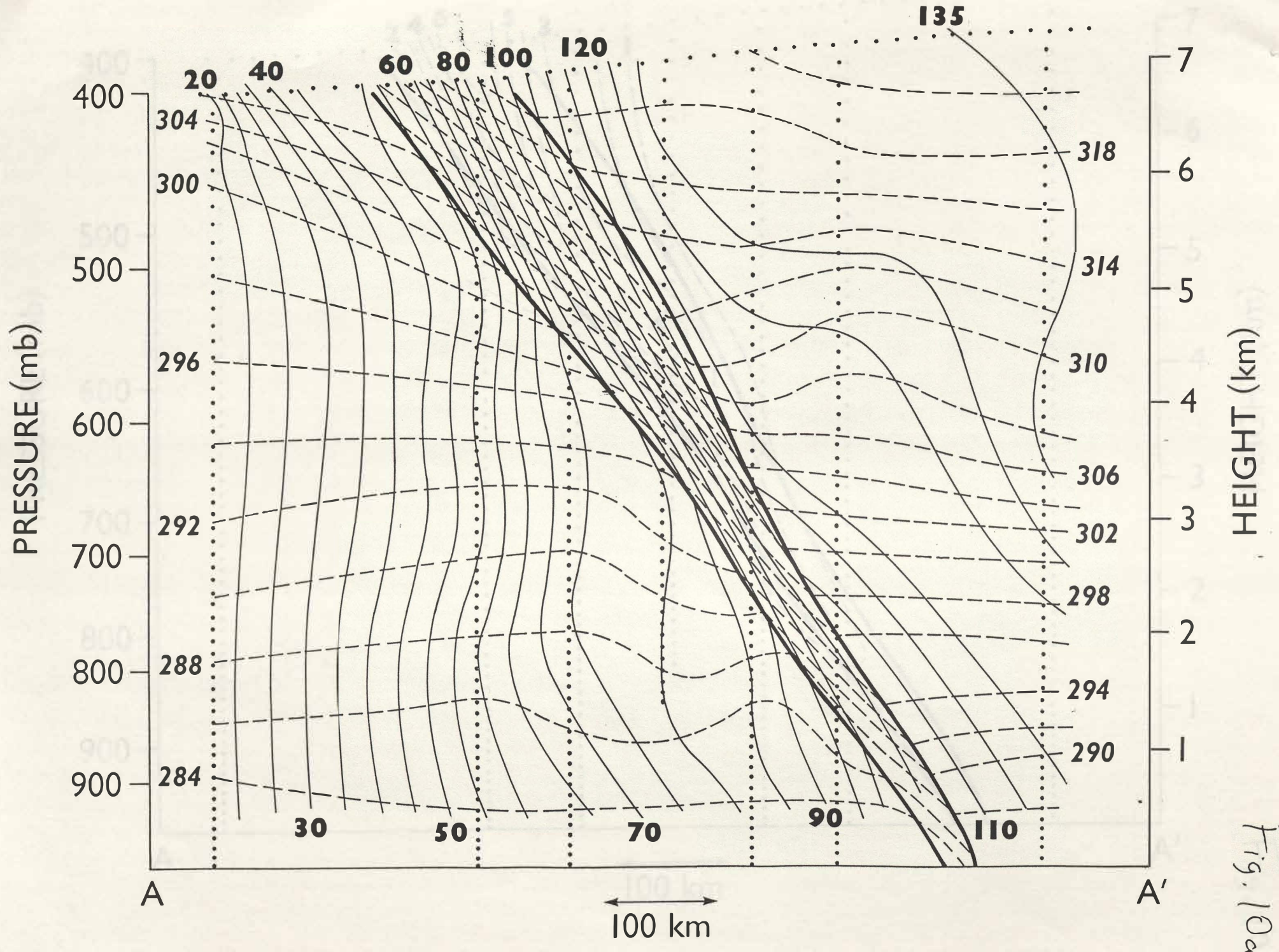


Fig. 10a

PRESSURE (mb)

400
500
600
700
800
900

HEIGHT (km)

7
6
5
4
3
2
1

A

A'

100 km

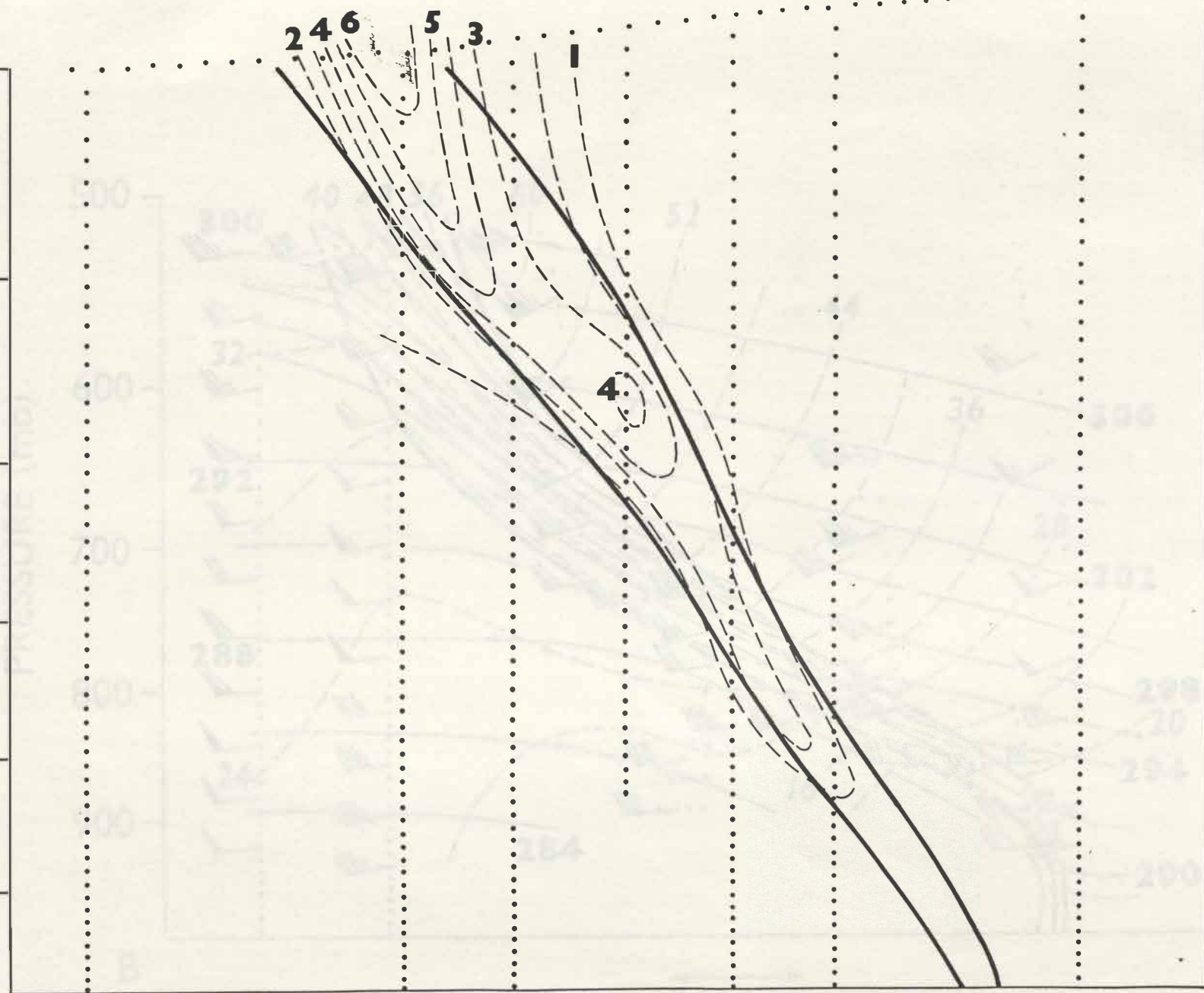


Fig. 106

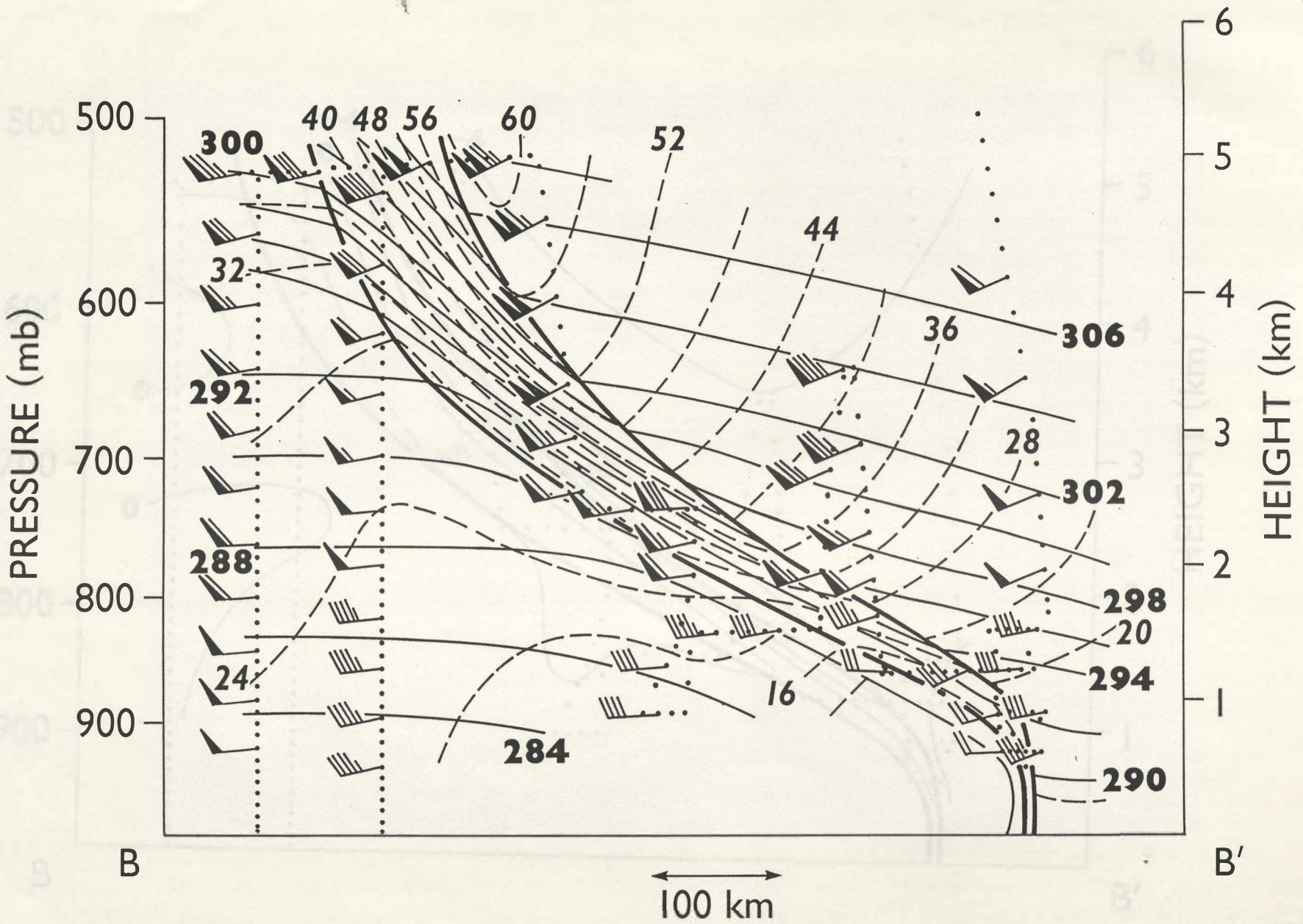


Fig. 11

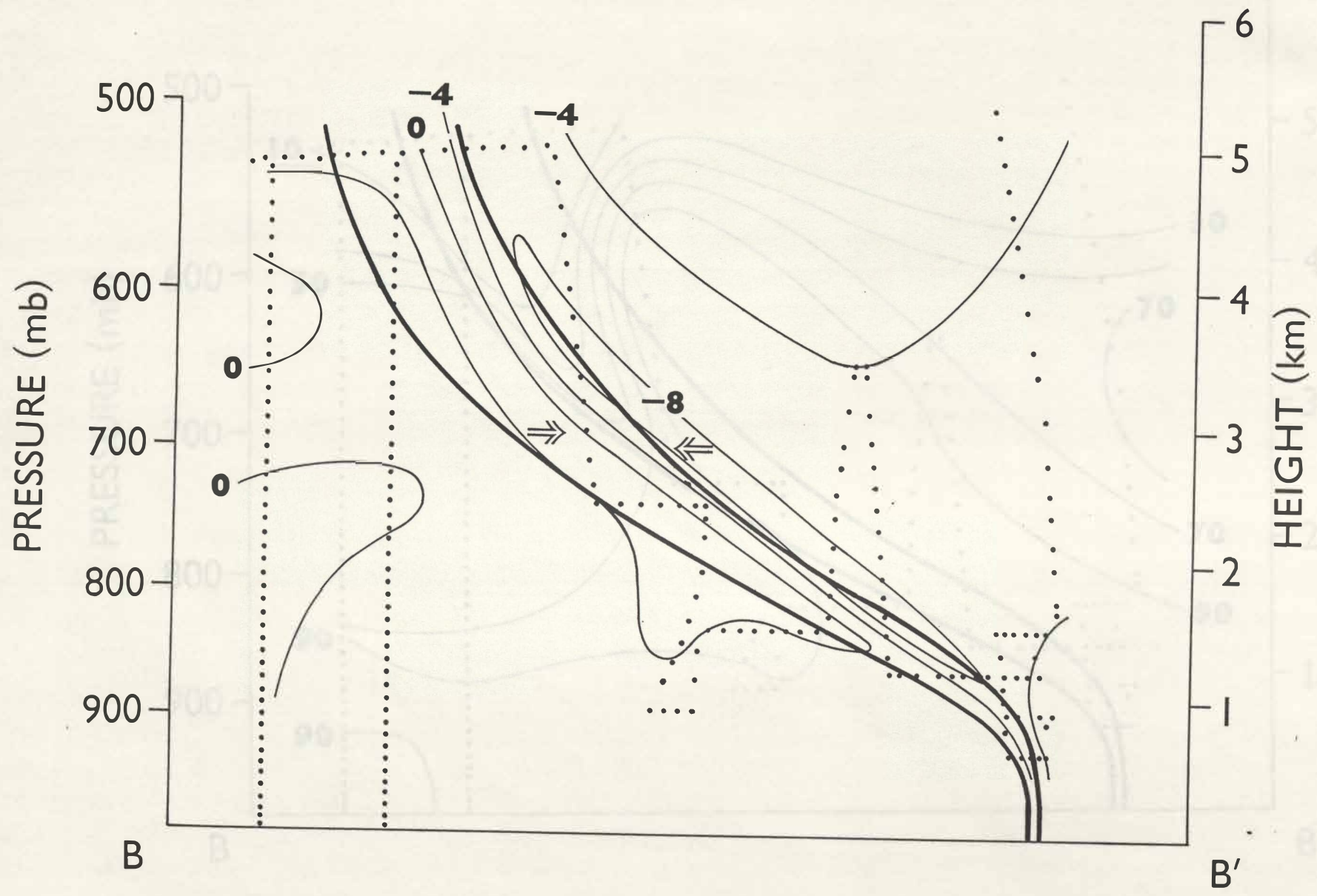


Fig. 12

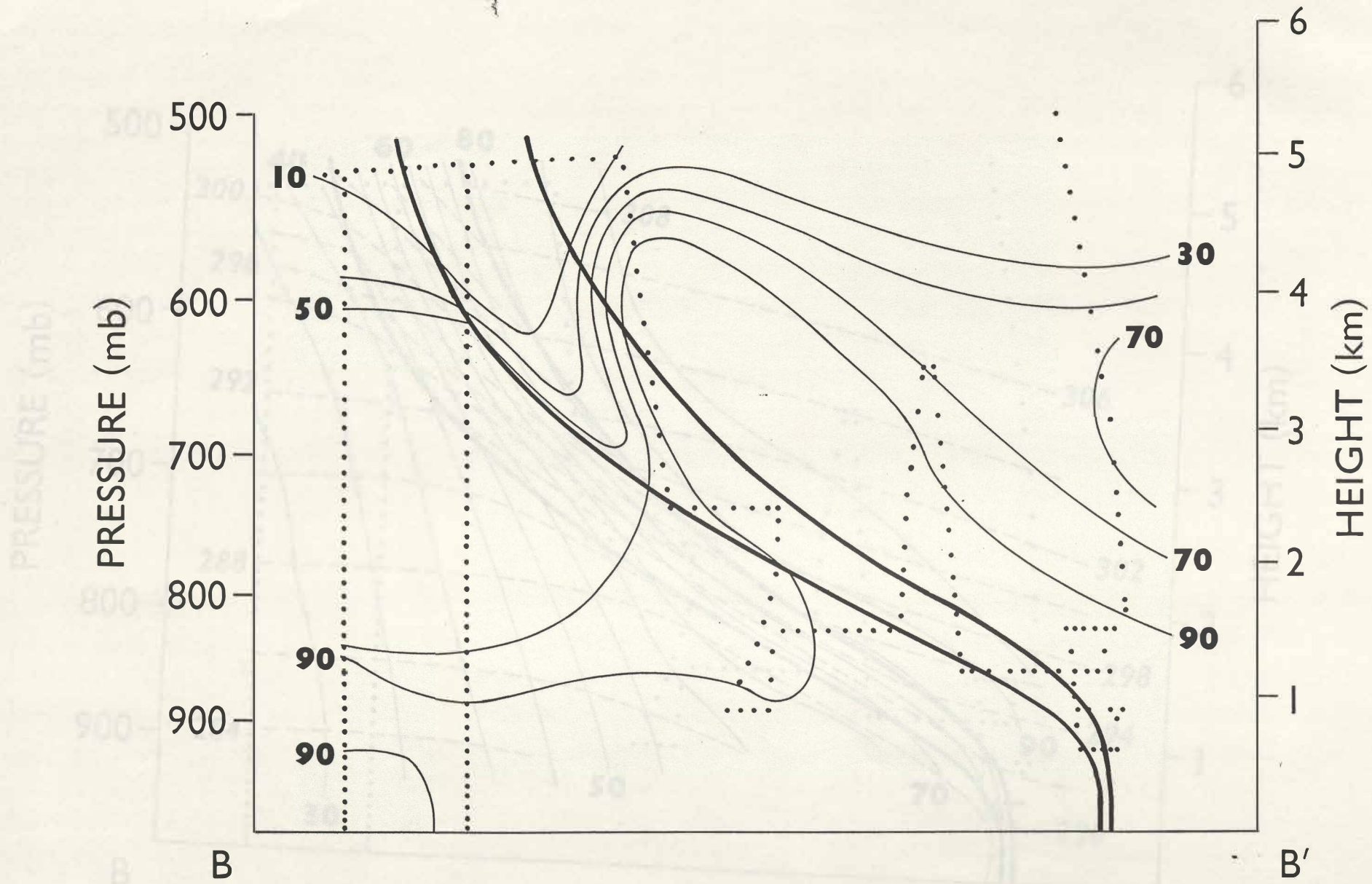


Fig. 13

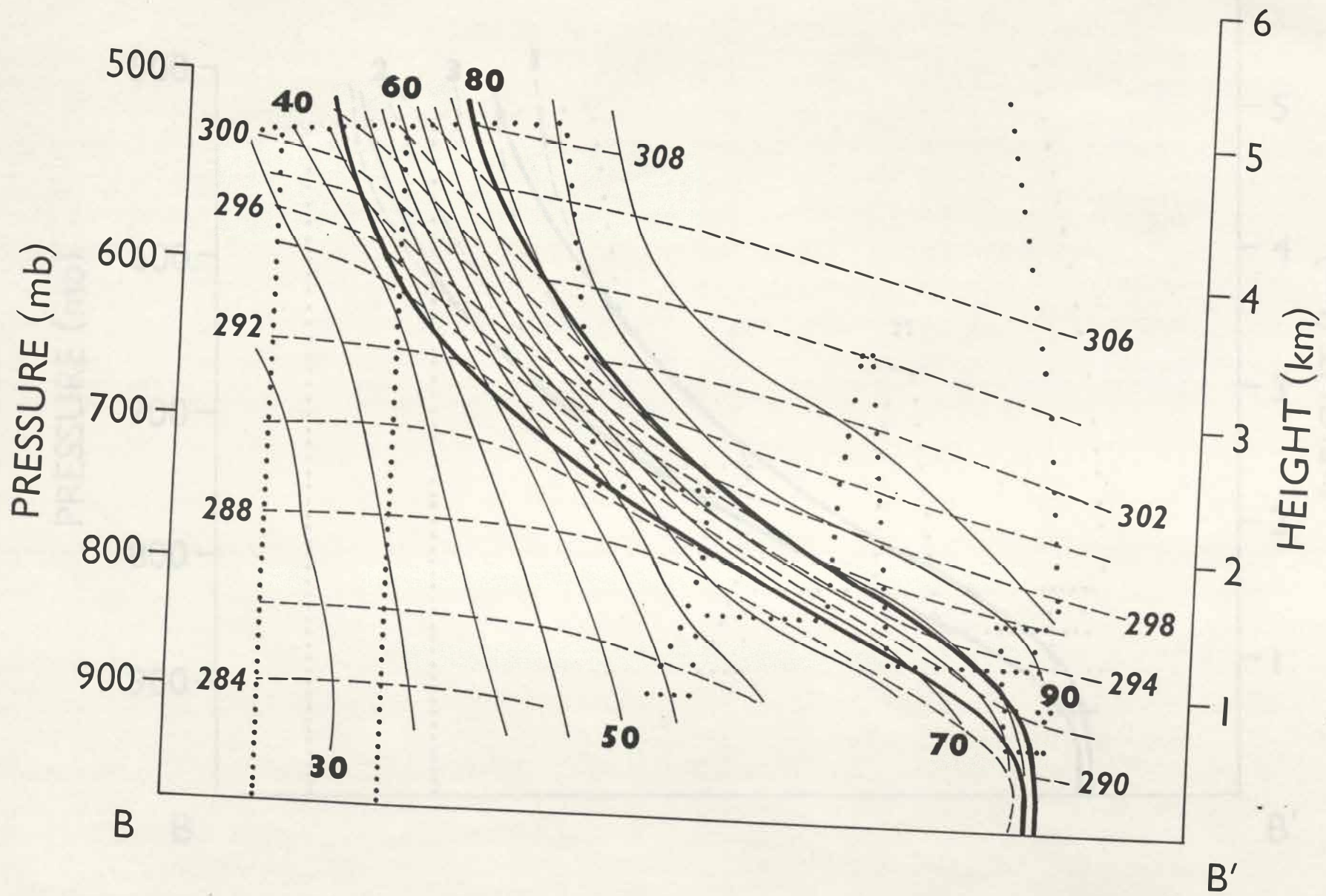


Fig. 14a

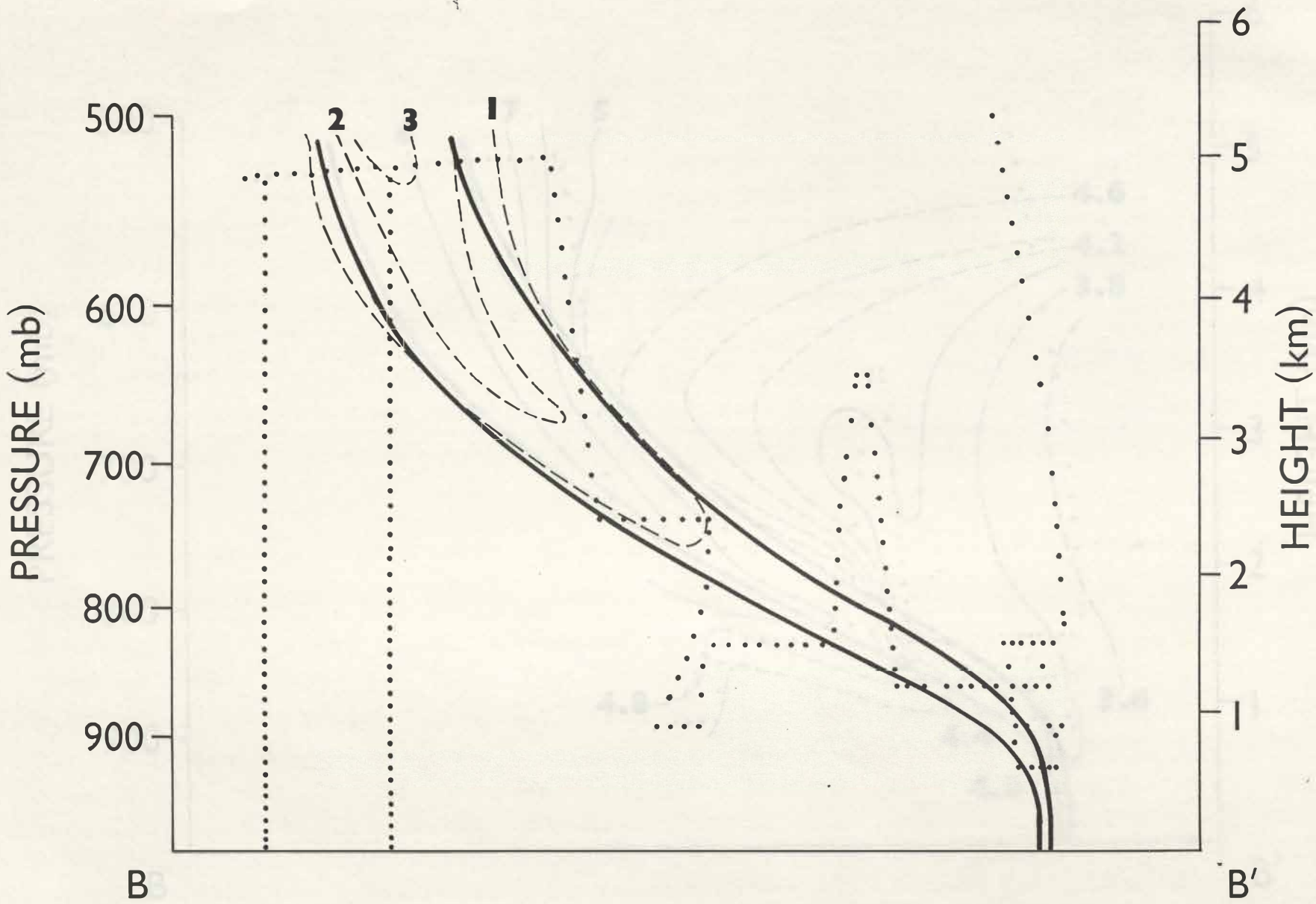


Fig. 146

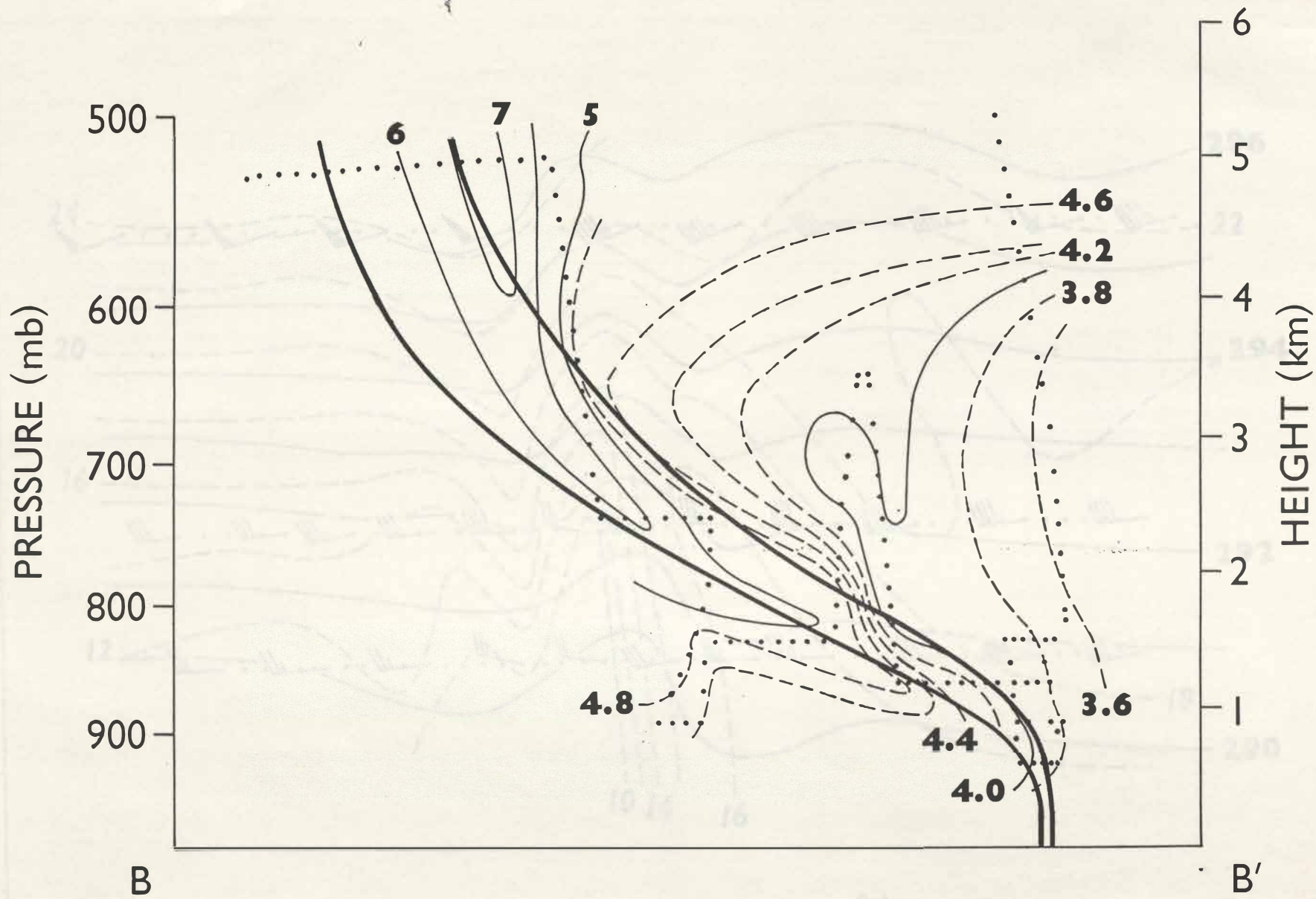


Fig. 15

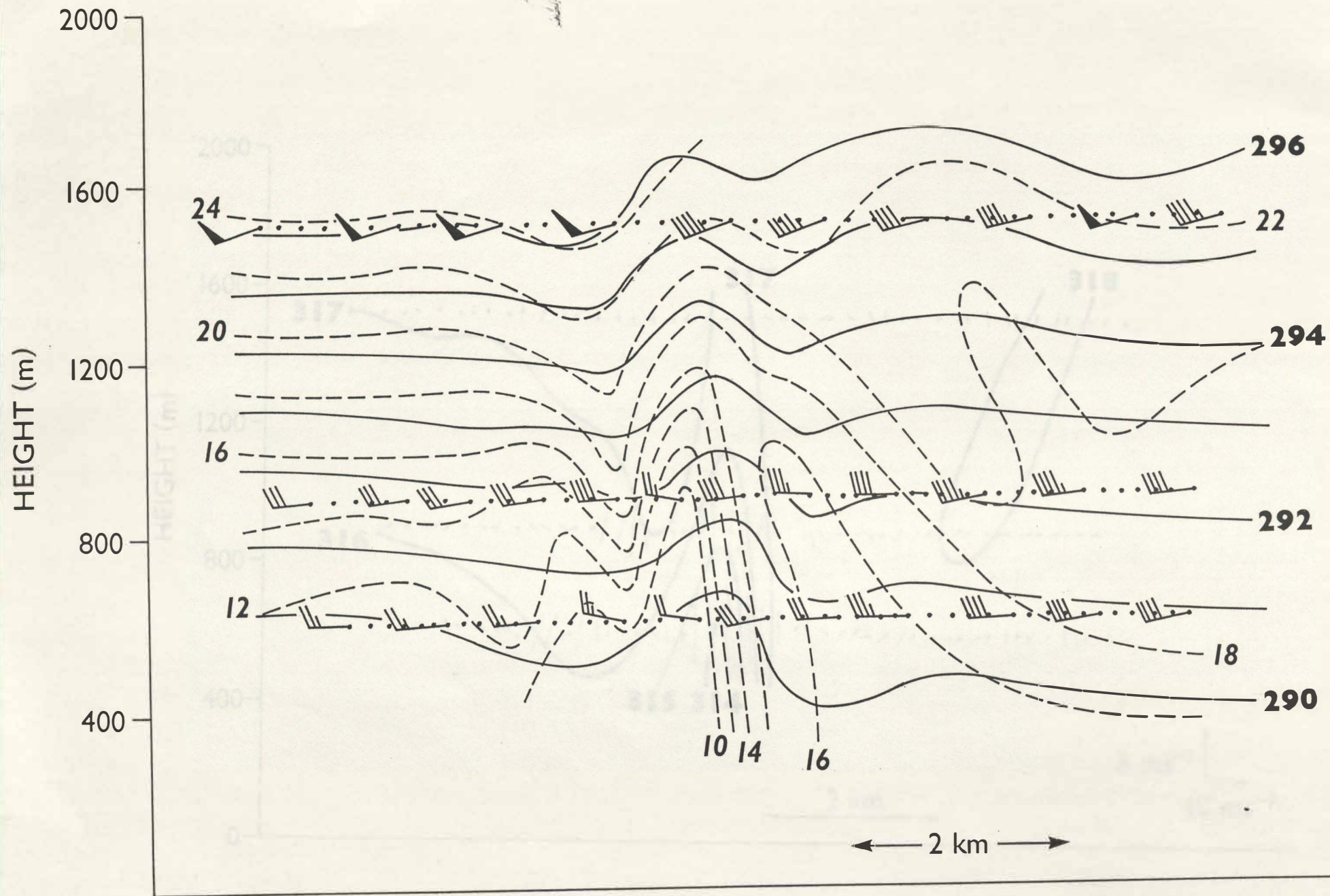


Fig. 16

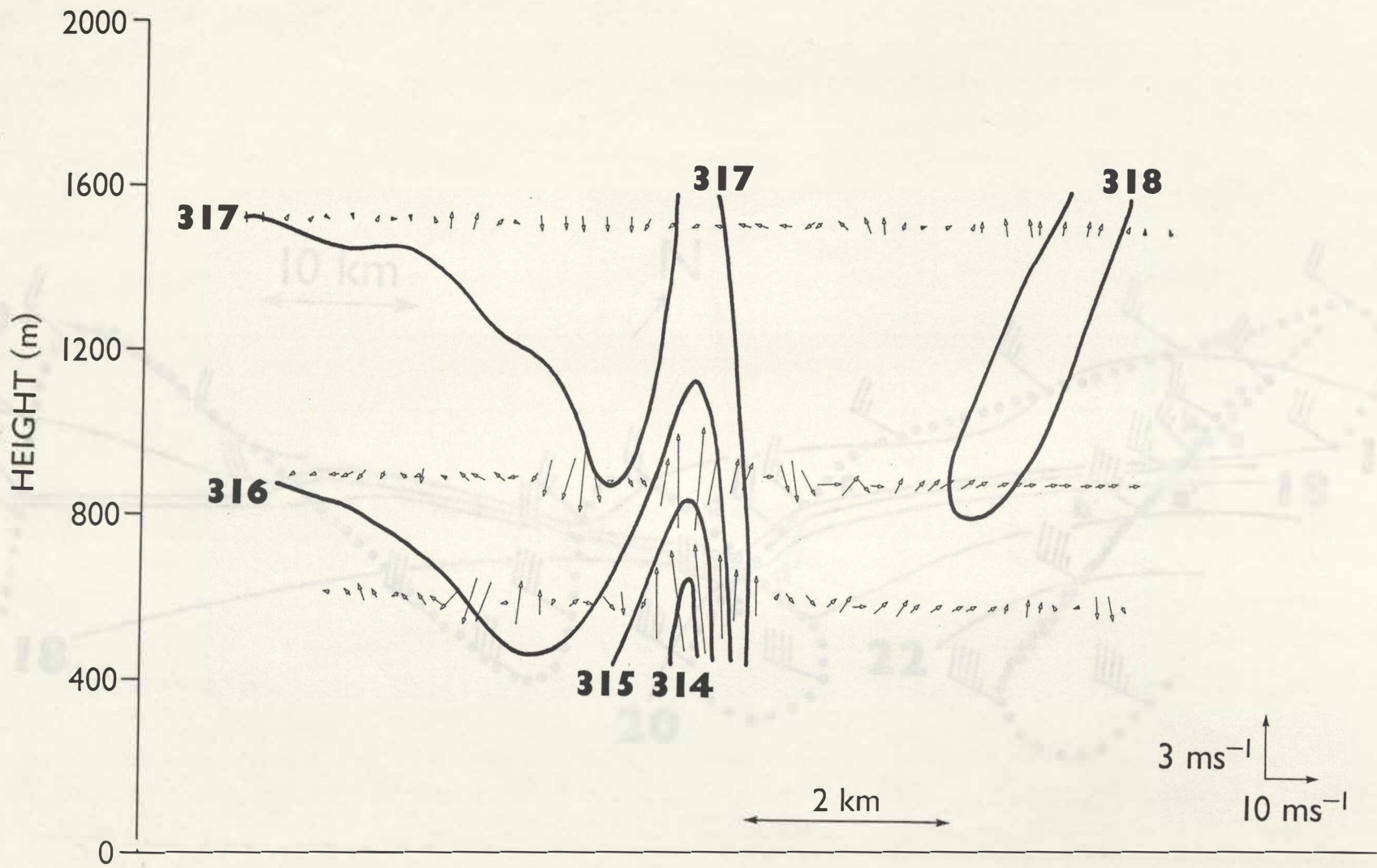


Fig. 17

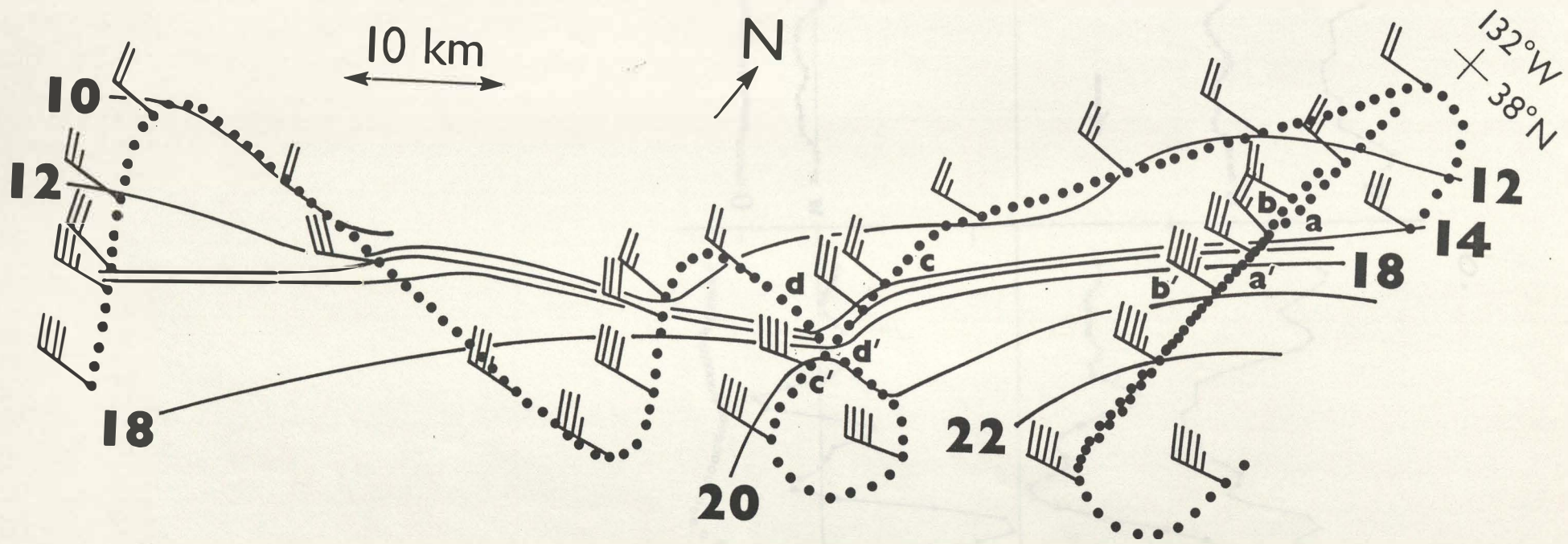
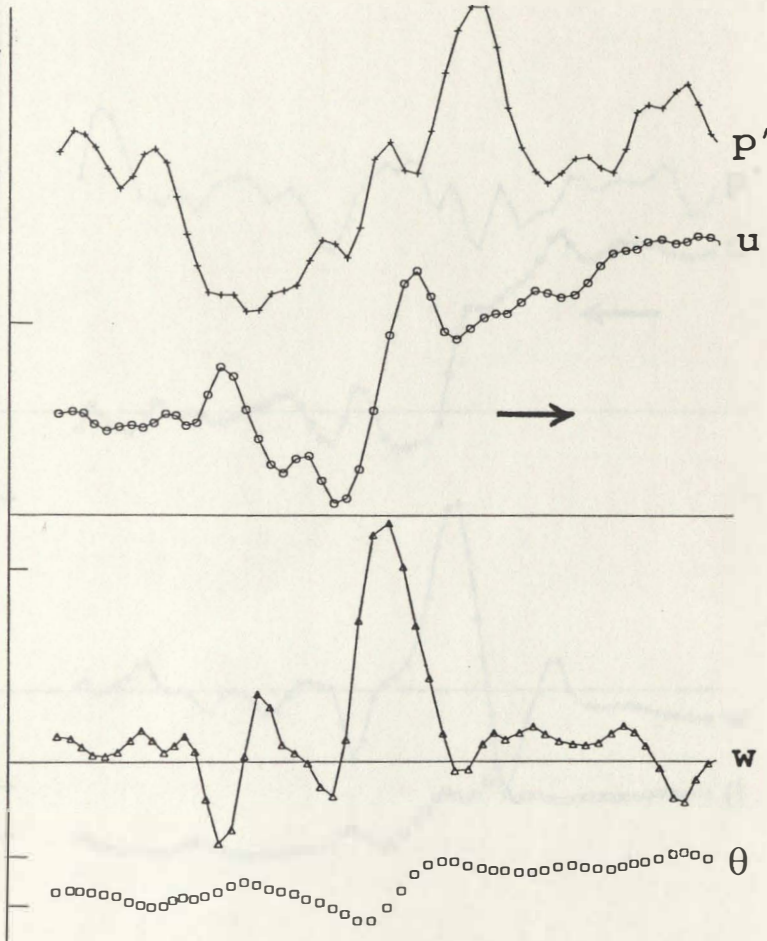
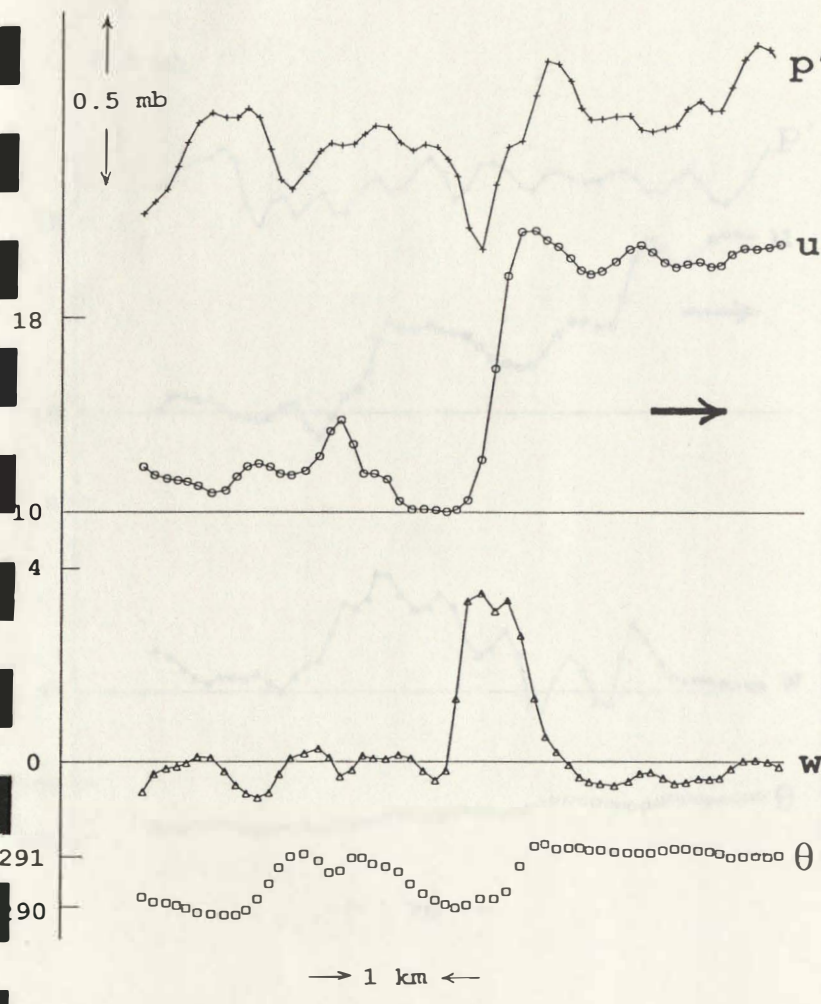


Fig. 18

Fig. 19

a.

b.



C.

D.

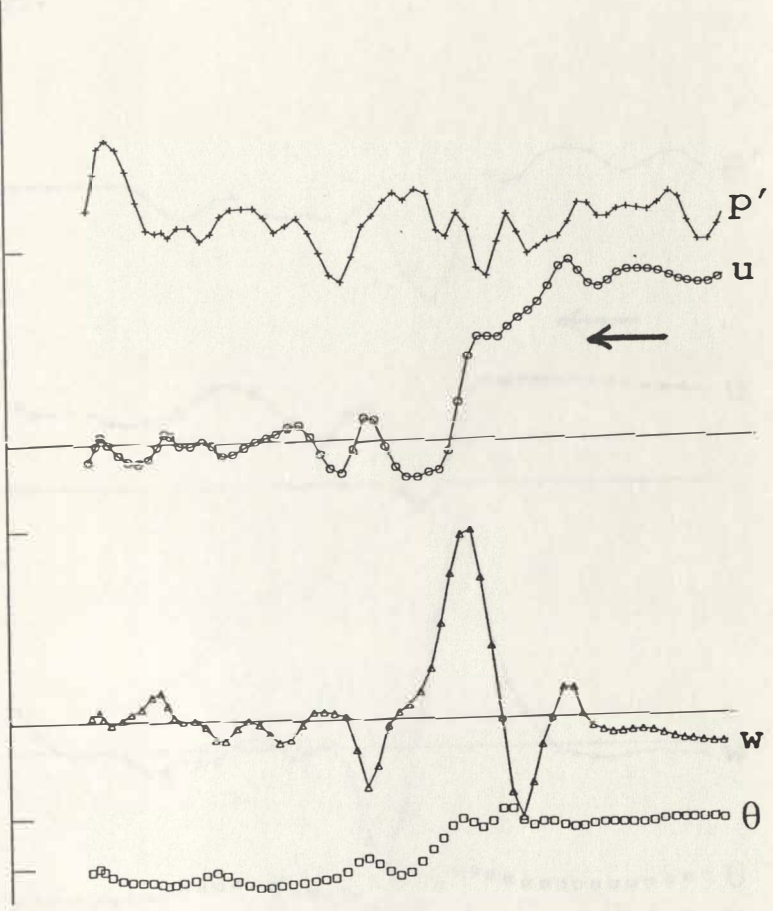
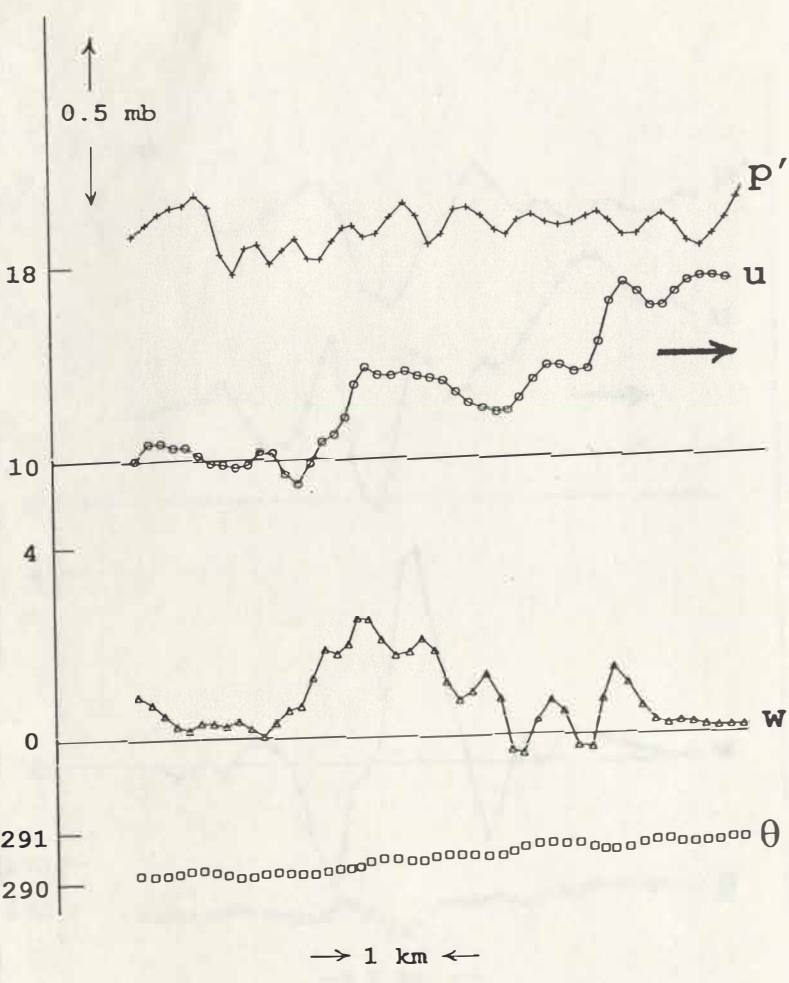
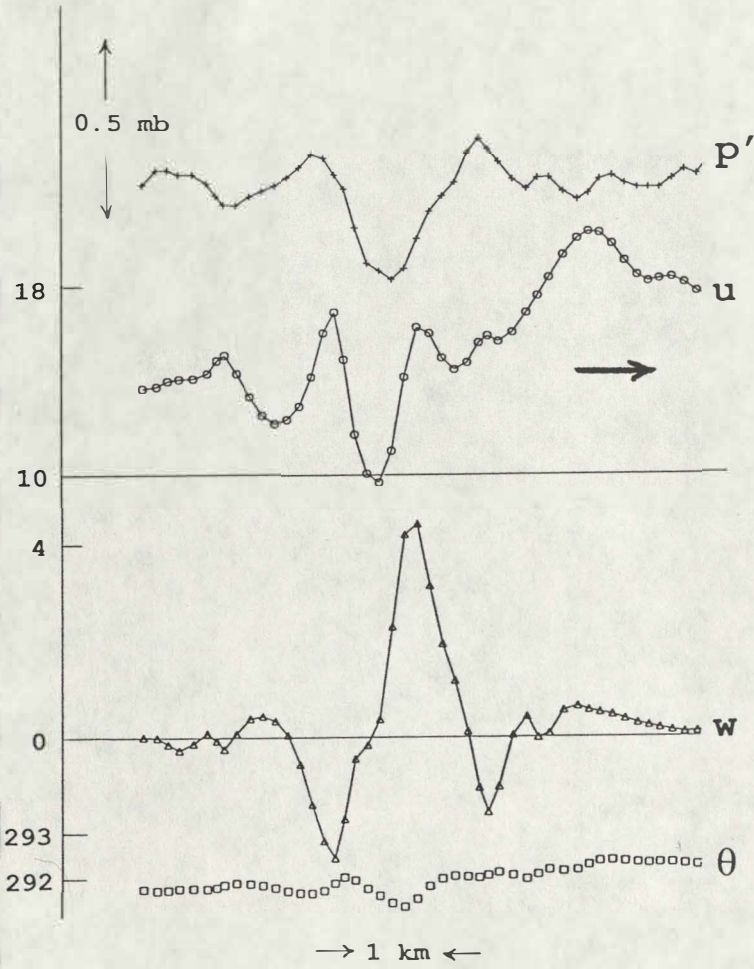


Fig. 20

a.



b.

